

# EES Catalysis

Accepted Manuscript

This article can be cited before page numbers have been issued, to do this please use: H. Iriawan, D. A. Haro, J. Adjei, D. Donneys Victoria, A. Ashley, A. J. Medford, M. C. Hatzell, G. G. Botte and Y. Shao-Horn, *EES Catal.*, 2026, DOI: 10.1039/D6EY00044D.



This is an Accepted Manuscript, which has been through the Royal Society of Chemistry peer review process and has been accepted for publication.

Accepted Manuscripts are published online shortly after acceptance, before technical editing, formatting and proof reading. Using this free service, authors can make their results available to the community, in citable form, before we publish the edited article. We will replace this Accepted Manuscript with the edited and formatted Advance Article as soon as it is available.

You can find more information about Accepted Manuscripts in the [Information for Authors](#).

Please note that technical editing may introduce minor changes to the text and/or graphics, which may alter content. The journal's standard [Terms & Conditions](#) and the [Ethical guidelines](#) still apply. In no event shall the Royal Society of Chemistry be held responsible for any errors or omissions in this Accepted Manuscript or any consequences arising from the use of any information it contains.

## Broader context

Electrified nutrient recovery from municipal waste streams is emerging as a promising strategy to transform wastewater treatment infrastructure into distributed platforms for circular fertilizer production. However, the complex and variable composition of these waste streams presents major challenges for catalyst evaluation, mechanistic understanding, and reliable product quantification. Amino acids are the key building blocks of proteins and dominant nitrogen-containing components of waste sludge. Yet even for the simplest amino acids, such as glycine, fundamental knowledge of nitrogen and carbon product distributions, selectivity, and catalyst stability remains limited. In this work, we establish a reproducible experimental framework across laboratories to examine glycine electrolysis and uncover unexpected ammonia formation as the dominant N product under strongly oxidative conditions, despite its sheer thermodynamic driving force to form oxidized products. Comprehensive characterization of reaction byproducts and systematic experimental evaluation provide key mechanistic insights into C–N bond cleavage and hydrogenation steps governing ammonia formation, while highlighting the critical influence of reaction environment and operating parameters on catalyst stability and selectivity. These findings lay the foundation for scalable electrochemical strategies to recover ammonia from organic waste streams, advancing circular nitrogen management and electrified waste treatment.



# Unraveling Electrochemical Glycine Conversion Pathways for Ammonia Recovery from Organic Waste

Haldrian Iriawan<sup>+\*1</sup>, Jedidian Adjei<sup>+2,3</sup>, Danae A. Haro Chipoco<sup>+4</sup>, Dayana Donneys Victoria<sup>3</sup>, Asa Ashley,<sup>5</sup> Andrew J. Medford<sup>\*6</sup>, Marta C. Hatzell<sup>\*7</sup>, Gerardine G. Botte<sup>\*2,3</sup>, Yang Shao-Horn<sup>\*1,5,8</sup>

<sup>1</sup>Department of Materials Science & Engineering, Massachusetts Institute of Technology, Cambridge, MA, 02139, United States

<sup>2</sup>Department of Chemical Engineering, Texas Tech University, Lubbock, TX 79409

<sup>3</sup>Institute for Sustainability Circular Economy, Texas Tech University, Lubbock, TX 79409

<sup>4</sup>School of Materials Science and Engineering, Georgia Institute of Technology, Atlanta, GA, 30332, USA

<sup>5</sup>Research Laboratory of Electronics, Massachusetts Institute of Technology, Cambridge, MA, 02139, United states

<sup>6</sup>School of Chemical & Biomolecular Engineering, Georgia Institute of Technology, Atlanta, GA, 30332, United States

<sup>7</sup>George W. Woodruff School of Mechanical Engineering, Georgia Institute of Technology, 770 Ferst Ave, Atlanta, GA, 30309, USA

<sup>8</sup>Department of Mechanical Engineering, Massachusetts Institute of Technology, Cambridge, MA, 02139, United States

<sup>+</sup>Equally contributing authors

<sup>\*</sup>Corresponding authors



## Abstract

Electrochemical conversion of nitrogen-containing organics in sludge offers a route for ammonia recovery but is challenged by compositional complexity. Glycine, abundant in municipal wastewater and structurally simple, provides a model system to benchmark nitrogen and carbon product distributions and electrode stability. Here, we report a coordinated cross-institutional study to elucidate glycine electro-oxidation pathways to ammonia. In alkaline electrolyte, ammonia was produced preferentially under oxidative potentials ( $>1.60 V_{\text{RHE}}$ ), rather than reductive conditions ( $< -0.40 V_{\text{RHE}}$ ), with Ni exhibiting lower overpotentials than Au and Pt. At  $2.00 V_{\text{RHE}}$ , ammonia was the dominant nitrogen product ( $\sim 70\%$ ), but with moderate Faradaic efficiency ( $23.5 \pm 2.5\%$ ), accompanied by  $\text{NO}_2^-/\text{NO}_3^-$  ( $\sim 24\%$ ), Ni dissolution ( $\sim 12\%$ ), and  $\text{O}_2$  evolution ( $\sim 40\%$ ), collectively closing the charge balance. Carbon analysis using HPLC, IC, and  $^{13}\text{C}$  NMR revealed a mix of glycolate, glyoxylate, formaldehyde, cyanide, and formate ( $\sim 20\%$  carbon,  $6\%$  faradaic efficiency), with the remainder as  $\text{CO}_2$ , indicating concurrent C-N and C-C cleavage pathways. These data, combined with thermodynamic analysis, inform a unified reaction framework and reveal C-N cleavage as the rate-limiting step. Furthermore, the ammonia-dominated production and coupled  $\text{Ni}^{2+}$  dissolution are correlated across other amino acids, highlighting Ni-complexation as a possible underlying mechanism favoring ammonia production. This work establishes a product-resolved framework and assesses experimental parameters (stirring, cell geometry, potential pulsing) to improve reproducibility and advance mechanistic understanding of ammonia recovery from organic nitrogen electrolysis.

## Introduction

Recovering ammonia from nitrogen-containing organic wastes is an increasingly attractive strategy to couple waste management with nutrient circularity. Municipal and agricultural waste streams contain substantial amounts of organically bound nitrogen that are removed during conventional biological treatments rather than recovered as fertilizer precursors.<sup>1</sup> As a widely implemented biological process, an activated sludge treatment entails enzymatic mineralization of organic-N to ammonium ( $\text{NH}_4^+$ ) via microbial hydrolysis and deamination.<sup>2</sup> The resulting  $\text{NH}_4^+$  is oxidized to nitrite/nitrate by microorganisms, followed by reduction to  $\text{N}_2$  (denitrification),<sup>2,3</sup> resulting in irreversible nitrogen loss and often requiring external electron donors such as carbon black to sustain complete denitrification.<sup>4</sup> The conventional activated sludge processes are also energy intensive, where aeration represents the dominant electricity demand (often reported as  $\sim 45\text{--}75\%$  of energy cost).<sup>5</sup>



Electrochemical approaches offer an attractive route in which chemical transformations are driven directly by applied potential and powered by electricity, enabling flexible operational control and coupling to renewables.<sup>6,7</sup> Compared to thermal routes for sludge conversion (e.g., pyrolysis/gasification), which typically operate at ~300 - 1000 °C and demand centralized heat integration and solid-handling infrastructure,<sup>8,9</sup> or plasma-assisted routes which rely on specialized reactors and high-energy excitation,<sup>10</sup> electrolysis can operate near ambient conditions and allows modular, decentralized deployment at wastewater treatment facilities.<sup>11</sup> Jafari and Botte demonstrate that the electrochemical treatment of waste-activated sludge can produce ammonia (NH<sub>3</sub>) alongside short-chain fatty acids using electrodes including Ni, Cu, and stainless steel at low potentials (~1.35 V versus Hg/HgO) in alkaline media (0.2 M NaOH), or ~2.2 V versus reversible hydrogen electrode assuming pH = 13.<sup>12</sup> Notably, Ni electrodes are reported to yield 250 mg L<sup>-1</sup> of ammonia after 2 h of pulsed electrolysis.<sup>12</sup> Technoeconomic analyses of electrically-assisted sludge conversion using these experimental findings reveal electrolysis as a promising route for sludge valorization and nutrient recovery, with potential advantages in integration simplicity, distributed operation, and compatibility with intermittent electricity.<sup>6</sup>

A central challenge in valorizing wastewater-derived feedstocks is that sludge composition varies widely with source, thus complicating product distribution and electrode stability analyses. In sewage sludge, the total solids (TS) content is typically 2-9%, of which organic solids account for approximately 20-44%.<sup>13</sup> Within this organic fraction, carbon constitutes roughly 20-40% of TS,<sup>13-16</sup> while total nitrogen is present at 2.8-4.9%.<sup>13,14,16,17</sup> Proteins represent a dominant component of the organic matter (40-60%)<sup>18</sup>, alongside polysaccharides, lipids, and fatty acids.<sup>19</sup> At alkaline conditions, proteins can be depolymerized into their constituent amino acids, and analyses of waste-activated sludge have identified ~18 amino acids with distinct compositional distributions (see **Table 1**).<sup>20</sup> As the highest nitrogen-density fraction of sludge, proteins and their amino acid building blocks are therefore attractive targets for electrochemical upgrading strategies aimed at ammonia recovery. Of these, glycine is a practical model molecule for two reasons: it is one of the most abundant amino acids in municipal sludge and extracellular polymeric substances, and it is the simplest amino acid, containing only an amine and a carboxylate group with no side chains. This minimal chemical complexity makes glycine an ideal benchmark system for isolating how experimental variables influence key observables such as nitrogen and carbon product distributions, faradaic efficiencies, and electrode stability.



Electrochemical glycine oxidation has been explored on a range of electrode materials, including Pt, Au and more recently Ni-based metals. The oxidation of glycine on Pt has been extensively investigated. For example, Marangoni et al. have studied glycine (at 0.45 M) on Pt at both pH 1 and 13 via cyclic voltammetry and constant potential measurements, whose findings lead to mechanisms involving glycine adsorption through the carboxyl group followed by CO<sub>2</sub> evolution or and methylamine to form ammonia and formaldehyde.<sup>21</sup> The ammonia yield at pH 13 at 1.06 V<sub>SCE</sub> (i.e. ~1.8 V<sub>RHE</sub>)<sup>21</sup> was reported at ~83%, although the number of electrons (n<sub>e</sub>) in the calculation was not specified and that the ammonia detection via the Kjeldahl method<sup>22</sup> could be interfered by organic N as well as NO<sub>2/3</sub><sup>-</sup>.<sup>23</sup> The proposed mechanism of glycine oxidation on Pt<sup>24</sup> and Au<sup>25</sup> is supported by in situ vibrational spectroscopy, revealing the glycine adsorption by the COO<sup>-</sup> down configuration and reaction intermediates such as CN<sup>-</sup> and CNO<sup>-</sup>, alongside reaction products such as CO<sub>2</sub> and NH<sub>3</sub>. However, the quantification of ammonia efficiency and product distribution is not reported. More recently, Ni-based electrodes that can convert surface Ni(OH)<sub>2</sub> (Ni(II)) to NiOOH (Ni(III)) upon oxidation and effectively oxidize urea<sup>26,27</sup> and alcohols,<sup>28</sup> are reported for glycine oxidation, including doped Ni(OH)<sub>2</sub> catalysts such as Ni<sub>0.77</sub>Co<sub>0.20</sub>Cd<sub>0.03</sub>(OH)<sup>29</sup> and Ni<sub>1.5</sub>Mn<sub>1.5</sub>O<sup>29</sup>. Furthermore, amino acid conversion to ammonia, including glycine, was reported to have enhanced charge efficiency by potential pulsing on Au and Ni,<sup>30</sup> an established strategy in enhancing the turnover of the desired products as demonstrated in CO<sub>2</sub> reduction to C<sup>2+</sup> products,<sup>31</sup> NO<sub>3</sub><sup>-</sup> reduction to NH<sub>4</sub><sup>+</sup>,<sup>32</sup> and urea oxidation.<sup>27</sup> Despite these reports, systematic analyses of reaction products generated during glycine oxidation on metals, electrode stability in the presence of glycine and N-containing ligands and the impact of experimental conditions on the measured faradaic efficiencies, is lacking.

**Table 1.** Amino acid composition of waste activated sludge<sup>20</sup>

Amino Acid	% of Total Amino Acids
Aspartic acid (Asp)	8.3
Glutamic acid (Glu)	8.1
Alanine (Ala)	7.3
Leucine (Leu)	5.6
Glycine (Gly)	4.9
Threonine (Thr)	4.2
Valine (Val)	4.1



Serine (Ser)	3.4
Lysine (Lys)	3.3
Proline (Pro)	3.1
Phenylalanine (Phe)	3.1
Arginine (Arg)	2.9
Isoleucine (Ile)	2.7
Tyrosine (Tyr)	2.4
Cystine (Cys)	2.1
Methionine (Met)	1.45
Tryptophan (Trp)	0.8
Histidine (His)	0.6

In this work, we have performed a coordinated cross-institution study to investigate experimental details of electrochemical glycine conversion to ammonia. Three independent labs at different institutions have executed a normally identical protocol spanning cell/component cleaning, electrode treatment, reference electrode calibration, electrochemical operation, and product quantification. With the shared benchmarking effort, using polished Ni foil in 0.1 M KOH + 0.1 M glycine, ammonia was detected under oxidative potentials ( $>1.60 V_{\text{RHE}}$ ). At  $2.00 V_{\text{RHE}}$ , ammonia dominates the solution-phase nitrogen products ( $\sim 70\%$  of the N-product distribution) with ammonia Faradaic efficiency of  $23.5 \pm 2.2\%$  across institutions, but this selectivity is accompanied by parasitic reactions including substantial Ni dissolution ( $>12\%$ ), formation of oxidized nitrogen products ( $\text{NO}_{2/3}^-$ ,  $\sim 24\%$ ), and  $\text{O}_2$  evolution ( $\sim 40\%$ ), cumulatively leading to complete faradaic efficiency. Comprehensive carbon analysis via high performance liquid chromatography (HPLC), ion chromatography (IC), and carbon nuclear magnetic resonance ( $^{13}\text{C}$ -NMR) revealed multiple oxidation products such as glycolate, glyoxylate, formaldehyde, cyanide, formate, and  $\text{CO}_2$  in the form of bicarbonate ( $\text{CO}_3^{2-}$ ) which contribute to a total of  $\text{FE} = \sim 6\%$ , indicating parallel pathways involving C=N and C-C scission in glycine activation. Furthermore, extending the study to alanine, lysine, and aspartic acid revealed that ammonia-dominated production was correlated with  $\text{Ni}^{2+}$  dissolution, highlighting Ni complexation as a possible origin of ammonia-dominated production. Critically, nitrogen selectivity, Ni corrosion rates, and carbon product distribution were found to depend on experimental conditions such as stirring rate, electrode area, cell architecture and potential pulsing, highlighting the strong influence of local reaction environment and underscoring the need for exhaustive reporting and community-facing best-practice protocols. Recommended



experimental practices are discussed to improve reproducibility and accelerate the mechanistic understanding of electrochemical amino acid conversion towards scalable ammonia recovery from organic waste.



## Experimental section

### Electrochemical glycine oxidation measurements

Nickel foil electrodes (0.25 mm thick, annealed, 99.5% metal basis, Thermo Scientific) cut into 1 x 0.5 cm<sup>2</sup> pieces were electropolished prior to electrochemical measurements via a two-electrode setup in 85% ortho-phosphoric acid (Sigma-Aldrich), with Ni foil as the working electrode and a Pt or Ti mesh as the counter electrode at 3.0 V for 5 min. The current recorded was around 30 mA. The foil was then thoroughly rinsed with ethanol, wiped clean, and dried at 60 °C. For testing with Pt (0.1 mm thick, 99.99% metal basis, Sigma) and Au (0.1 mm thick, 99.95% metal basis, Thermo Scientific), the electrodes were sonicated in deionized water and dried overnight prior to use.

Electrochemical glycine oxidation experiments were conducted in a two-compartment H-cell, separated by an anion exchange membrane (DSVN, thickness = 95 μm, Bellex International Corp.) with both compartments containing 0.1 M as-received KOH (semiconductor grade, 99.99% trace metals basis, Sigma Aldrich) and 0.1 M Glycine (≥ 99%, Sigma Aldrich). Hg/HgO or Ag/AgCl reference electrodes were employed, and a Pt mesh (99.99%, StonyLab) served as the counter electrode. Prior to glycine experiments, the Ni working electrode was electrochemically conditioned by cycling through the oxygen evolution region (1.10–1.70 V<sub>RHE</sub>) for 25 cycles in glycine-free electrolyte (0.1 M KOH). Then, electrolytes were replaced and the working electrode compartment was bubbled with Ar (99,999%, Airgas or Linde) for 20 mins at 20 sccm before the start of electrolysis, where the step-by-step protocol can be found in **Supplementary Note 1**. The potentials reported against RHE follow Eq. 1, where the electrolyte pH was consistently measured to be 10.7 via a pH meter. To maintain a consistent applied potential during the potential holds and to prevent overcompensation at high currents caused by auto compensation (an issue previously reported),<sup>33</sup> the voltage was manually corrected for the IR drop. The solution resistance used for this correction was determined from the high-frequency real-axis intercept obtained by impedance spectroscopy measurements conducted after 15 minutes, 30 minutes, 1 hour, and 2 hours of electrolysis. The applied electrochemical potentials were converted to the reversible hydrogen electrode scale (V<sub>RHE</sub>) using the following equation:

$$V_{\text{RHE}} = V_{\text{meas}} + V_{\text{ref}} + 0.059 * \text{pH} - IR \quad (1)$$

where V<sub>meas</sub> is the potential difference measured between the working electrode and the reference electrode used during electrolysis, V<sub>ref</sub> is the potential difference between the standard hydrogen electrode and the reference electrode use in the experiments (i.e. +0.210 V for Ag/AgCl 3 M KCl, +0.197 V for Ag/AgCl (sat. KCl) or +0.098 V for Hg/HgO with 4.24 M KOH at 25 °C)<sup>34</sup>, and IR the potential drop from solution resistance. We note that the RHE conversion via pH has been chosen over the HER/HOR method on Pt due to the apparent surface poisoning of Pt by glycine, which shifted the zero-current intercept (see discussion in **Supplementary Note 2** and **Figure S1**). During electrolysis, the working compartment was stirred with a PTFE 10 mm stir bar with a 3 mm diameter at 300 rpm. 3.0 mL of electrolytes were sampled at the 15 min, 30 min, 1 h and 2 h



intervals with replacement. Between experiments, the H-cell was thoroughly rinsed with deionized water (18.2 M $\Omega$  cm, Millipore) and dried, while the membrane was stored in deionized water. Periodic deep cleaning was performed approximately monthly by overnight (12h) soaking in aqua regia, followed by boiling at >200 °C for > 30 mins in deionized water. Other amino acids tested were 0.1 M Lysine (L, Sigma,  $\geq$  98%), 0.1 M Alanine (L, Sigma,  $\geq$  99.5% BioUltra) and 0.1 M Alanine (L, Sigma,  $\geq$  99.5% BioUltra) and 0.05 M Aspartic acid (L, 99%, BioXtra), where the experimental procedure was identical to that of glycine.

### Product quantification

**Ammonia (NH<sub>3</sub>)** in the glycine electrolyte was quantified as ammonium (NH<sub>4</sub><sup>+</sup>) using nuclear-magnetic resonance (NMR) and ion-chromatography (IC). We note that the presence of glycine significantly suppressed the blue color formation of the indophenol blue in the presence of ammonia, (**Figure S2**), rendering it ineffective for reliable quantification. Both H-NMR and IC quantification to be reliable (see calibration curves in **Figure S3-S7**). Therefore, ammonia quantification was managed independently at each laboratory, while cross-validation was performed at the Faradaic efficiency level considering the likely larger contributions of error from other experimental errors such as variations in the iR-corrected potential during electrolysis and electrode and analyte preparations (e.g. dilution errors).

**Nuclear-magnetic resonance.** At Institution 1, NH<sub>4</sub><sup>+</sup> was quantified via <sup>1</sup>H-NMR using 500.18 MHz Bruker AVANCE NEO spectrometer. 500  $\mu$ L of the analyte were mixed with 50  $\mu$ L of 4.0 M HCl, 25  $\mu$ L of 3 mM maleic acid and 63.9  $\mu$ L D<sub>2</sub>O. Acquisition of <sup>1</sup>H-NMR spectra was performed using the solvent suppression program with 128 scans and 2 s delay per scan. NH<sub>4</sub><sup>+</sup> calibration curve used for quantification and representative spectra post-electrolysis can be found in **Figure S3-4**. Ammonia in the acid trap was generally found to be minimal, 2 orders of magnitude lower than the ammonia in the electrolyte (see **Figure S5**). Therefore, the faradaic efficiencies reported utilized ammonia in the electrolyte.

**Ion-chromatography.** The specific instrument column configurations at Institutions 2 and 3 can be found in **Supplementary Information**, each yielding reliable NH<sub>4</sub><sup>+</sup> calibration (**Figure S6-S7**) prepared from ammonium standards (99.999% NH<sub>4</sub>Cl, VeriSpec®). At Institution 2, electrolysis samples were acidified with 1 M HCl and diluted 100 times with DI water, and the samples were measured with 15 mM methanesulfonic acid eluent at 0.25 mL/min at 25 °C. At Institution 3, samples were detected without acidification and dilution, and measured with 30 mM methanesulfonic acid as the eluent at 30 °C. The acquisition and evaluation of chromatograms were carried out with the software Chromeleon (Thermo Scientific).

**Nitrate (NO<sub>3</sub><sup>-</sup>) and nitrite (NO<sub>2</sub><sup>-</sup>).** All three institutions employed anion chromatography with a conductivity detector, where the specific instrument column configurations can be found in **Supplementary Information** and independently yielded a linear calibration curve against NO<sub>3</sub><sup>-</sup> and NO<sub>2</sub><sup>-</sup> standards of known concentrations (**Figure S8-S9**). At Institution 1, 250  $\mu$ L samples were diluted by a factor of 2 with deionized water and measured at 0.25 mL/min of sodium



carbonate and bicarbonate eluent. At Institution 2, samples were diluted 100 times with deionized water and measured at 0.15 mL/min of the same eluent. At Institution 3, 25  $\mu\text{L}$  of sample of standard solution was injected into the eluent stream. The flow rate was maintained at 1.0 mL/min under a linear gradient elution from 20 mM to 40 mM KOH.

**Ni dissolution** was measured via Inductively-Coupled Plasma-Mass Spectrometry (ICP-MS, Institution 1) and ICP-OES (Institutions 2 and 3), where linear calibration curves with regard to  $\text{Ni}^{2+}$  concentration (ICP standard) were achieved (**Figure S10**) and independently generated for each ICP measurement. Samples were diluted with a factor of 5-500 in in 2%  $\text{HNO}_3$  (ICP grade).

**Gas quantification** was performed by connecting the H-cell to a SpectroInlet Electrochemistry Mass Spectrometer (EC-MS) Professional, which was equipped with a Quadrupole Mass Spectrometer (QMG 250, Pfeiffer). A Spectro Inlet aqueous chip enabled gaseous products to enter the mass spectrometer, with all other openings sealed except the connection to the H-cell (**Figure S11**). During operation, Ar was continuously flowed through the system at  $30 \text{ mL min}^{-1}$ . Prior to measurements, signals were recorded for 10 min to establish a stable baseline, after which the electrochemical program was initiated. For quantification, an  $\text{O}_2$  calibration curve was constructed by performing oxygen evolution on Ni foil in 0.1 M KOH. Constant current steps (30, 20, 10, 5, and 2.5 mA) were applied, with open-circuit intervals between each step to allow signal to decay back to the baseline level. The mass spectrometry signal at  $m/z = 32$  was then correlated with the expected  $\text{O}_2$  production (assuming 100% faradaic efficiency with  $z_e = 4$ , see **Table 2**) to generate calibration curves for both  $\text{O}_2$  production rate ( $\mu\text{mol s}^{-1}$ ) and total  $\text{O}_2$  evolved ( $\mu\text{mol}$ ), exhibiting excellent linearity (see **Figure S12**). This calibration was subsequently used to convert OER signals obtained during amino acid oxidation.

**Carbon products** were independently detected at the three institutions to qualitatively determine key reaction byproducts during glycine electrolysis. At Institution 1,  $^{13}\text{C}$ -NMR was employed for which the glycine electrolysis was performed following the same electrochemical protocol but instead used  $^{13}\text{C}_2$  glycine (99 atom%  $^{13}\text{C}$ , Sigma) where the two carbons are labelled. 500  $\mu\text{L}$  sample was mixed with 50  $\mu\text{L}$   $\text{D}_2\text{O}$  and measured with 500.18 MHz Bruker AVANCE NEO spectrometer. Spectra were acquired using a zgdepq pulse sequence with broadband  $^1\text{H}$  decoupling. A total of 512 scans were accumulated with a relaxation delay of 1.0 s over a spectral width of 30 kHz ( $\sim 240$  ppm), centered at 100 ppm. At institution 2, High-performance liquid chromatography was used with HPX-87H organic acid analysis column (AMINEX) paired with Biorad, equipped with a UV-vis detector positioned at 260nm (2489 UV/Vis Detector, Waters). The eluent was 5mM  $\text{H}_2\text{SO}_4$ , the column flow rate was 0.4mL/min and the column temperature was  $30^\circ\text{C}$ . At institution 3, anion chromatography was used to identify and quantify detected carbon products such as glycolate, formate, acetate, glyoxylate and oxalate using gradient elution, where the temperature ( $30\text{-}50^\circ\text{C}$ ) and elution time and KOH concentrations for linear gradient were optimized for each carbon product which resulted in linear calibration curves (**Figure S13**). Full details of instrument configuration can be found in the **Supplementary Information**. Cyanide quantification was done with Pyridine barbituric acid method (see **Supplementary Information**).



Chemical Oxygen Demand (COD) was attempted but suffered from significant interference from glycine, glyoxylic acid and formic acid (see **Supplementary Information** and **Figure S14**).

### Faradaic efficiency calculations

The Faradaic efficiency (FE) of N-products ( $\text{NH}_3$ ,  $\text{NO}_2^-$ , and  $\text{NO}_3^-$ ), metal products (Ni), and C-products were calculated by the following equation:

$$FE_i = \frac{z_i * n_i * F}{Q} \quad (2)$$

where  $z_i$  is the number of electrons used for the transformation assume complete oxidation of the carbon to  $\text{CO}_2$  for the nitrogen conversions to act as an upper-bound, as specified in **Table 2**;  $n_i$  is the number of moles of product  $i$ ,  $F$  is the Faraday constant ( $96484 \text{ C mol}^{-1}$ ), and  $Q$  is the amount of charge transferred during the reaction.

**Table 2.**  $z$  per product for FE calculations from electrochemical glycine oxidation

\*Since glycolic acid/glycolate is a 2-electron reduction from glyoxylic acid/glyoxylate,  $n_e=2$  for the glycine-to-glyoxylate

Compound	$z$	Equations
Ni	2	$\text{Ni}_{(s)} \rightarrow \text{Ni}^{2+} + 2e^-$
$\text{NH}_3$	6	$\text{NH}_2\text{CH}_2\text{COOH} + 2\text{H}_2\text{O} \rightarrow \text{NH}_3 + 2\text{CO}_2 + 6\text{H}^+ + 6e^-$ (acid) $\text{NH}_2\text{CH}_2\text{COO}^- + 5\text{OH}^- \rightarrow \text{NH}_3 + 2\text{CO}_2 + 3\text{H}_2\text{O} + 6e^-$ (alkaline)
$\text{NO}_2^-$	12	$\text{NH}_2\text{CH}_2\text{COOH} + 4\text{H}_2\text{O} \rightarrow \text{NO}_2^- + 2\text{CO}_2 + 13\text{H}^+ + 12e^-$ $\text{NH}_2\text{CH}_2\text{COO}^- + 12\text{OH}^- \rightarrow \text{NO}_2^- + 2\text{CO}_2 + 8\text{H}_2\text{O} + 12e^-$
$\text{NO}_3^-$	14	$\text{NH}_2\text{CH}_2\text{COOH} + 5\text{H}_2\text{O} \rightarrow \text{NO}_3^- + 2\text{CO}_2 + 15\text{H}^+ + 14e^-$ $\text{NH}_2\text{CH}_2\text{COO}^- + 14\text{OH}^- \rightarrow \text{NO}_3^- + 2\text{CO}_2 + 9\text{H}_2\text{O} + 14e^-$
$\text{O}_2$	4	$2\text{H}_2\text{O} \rightarrow \text{O}_2 + 4\text{H}^+ + 4e^-$ $4\text{OH}^- \rightarrow \text{O}_2 + 2\text{H}_2\text{O} + 4e^-$
$\text{CN}^-$	4	$\text{NH}_2\text{CH}_2\text{COOH} \rightarrow \text{CN}^- + \text{CO}_2 + 5\text{H}^+ + 4e^-$ $\text{NH}_2\text{CH}_2\text{COO}^- + 4\text{OH}^- \rightarrow \text{CN}^- + \text{CO}_2 + 4\text{H}_2\text{O} + 4e^-$
Glyoxylic acid	2	$\text{NH}_2\text{CH}_2\text{COOH} + \text{H}_2\text{O} \rightarrow \text{OCH-COOH} + \text{NH}_3 + 2\text{H}^+ + 2e^-$ $\text{NH}_2\text{CH}_2\text{COO}^- + 2\text{OH}^- \rightarrow \text{OCH-COO}^- + \text{NH}_3 + \text{H}_2\text{O} + 2e^-$
Glycolic acid	2*	$\text{OCHCOOH}_{(\text{glyoxylic acid})} + 2\text{H}^+ + 2e^- \rightarrow \text{HOCH}_2\text{COOH}_{(\text{glycolic acid})}$ (net) $\text{NH}_2\text{CH}_2\text{COOH} + \text{H}_2\text{O} \rightarrow \text{HOCH}_2\text{COOH} + \text{NH}_3$ (net) $\text{NH}_2\text{CH}_2\text{COO}^- + \text{H}_2\text{O} \rightarrow \text{HOCH}_2\text{COO}^- + \text{NH}_3$
Formic acid	4	$\text{NH}_2\text{CH}_2\text{COOH} + 2\text{H}_2\text{O} \rightarrow \text{HCOOH} + \text{CO}_2 + \text{NH}_3 + 4\text{H}^+ + 4e^-$ $\text{NH}_2\text{CH}_2\text{COO}^- + 4\text{OH}^- \rightarrow \text{HCOO}^- + \text{CO}_2 + \text{NH}_3 + 2\text{H}_2\text{O} + 4e^-$

conversion has been used in the Faradaic efficiency calculation of glycolate



## Results and discussion

### Benchmarking of electrochemical glycine oxidation

A shared electrochemical protocol, executed independently across three different laboratories, hereafter referred to as Institution 1-3 (**Figure 1a**), revealed ammonia as the dominant product of glycine electrolysis on nickel (Ni) at oxidative potentials. To enable meaningful benchmarking across laboratories, several experimental checkpoints were enforced prior to glycine electrolysis, which included consistent and overlapping cyclic voltammograms of Ni foil in the glycine-containing electrolyte (**Figure S15**) as well as aligned RHE potential conversion after iR correction (see demonstration in **Figure S16**). The latter required the consideration of solution resistance, which depended on the H-cell assembly, the accurate pH measurements of the glycine-containing electrolytes and rigorous reference electrode calibration (see **Supplementary Note 2** and **Figure S1**). Under these conditions, electrolysis at 2.00 V<sub>RHE</sub> after iR-correction (with variations of on average  $\pm 30$  mV over the 2 hours, see **Figure S17-S119** and **Table S1**) in 0.1 M KOH and 0.1 M glycine consistently produced ammonia as the predominant nitrogen-containing product across all three institutions. Specifically, NH<sub>3</sub> accounts for approximately 60-70% of the solution-phase nitrogen product distribution, while the remaining  $\sim 30\%$  consists of NO<sub>3</sub><sup>-</sup> and NO<sub>2</sub><sup>-</sup> (**Figure 1b**). These observations are robust across independent repeats at each institution, demonstrating agreement in the production levels of NH<sub>3</sub>, NO<sub>2</sub><sup>-</sup> and NO<sub>3</sub><sup>-</sup> (**Figure S20-S22**). In addition, by connecting the H-cell to a mass spectrometer (**Figure S13**), only O<sub>2</sub> (m/z = 32) was detected while other gas-phase products such as N<sub>2</sub> or CO (m/z = 28), NO (m/z = 30), and CO<sub>2</sub> (m/z = 44), were not observed above experimental uncertainty (**Figure S20**). The last was found to instead reside in the electrolyte as CO<sub>3</sub><sup>2-</sup>, which was characterized further (see ‘carbon product characterization’ section). We note that one aspect not initially controlled in the benchmarking was the stir bar size, which was found to considerably influence product selectivity (see later section). The formation of oxidized nitrogen species is not unexpected given the highly oxidative potential applied, which exceeded the thermodynamic redox potential of NH<sub>3</sub>/NO<sub>3</sub><sup>-</sup> ( $E^0 = 0.88$  V<sub>RHE</sub>)<sup>35</sup> and N<sub>2</sub>/NO<sub>3</sub><sup>-</sup> ( $E^0 = 1.24$  V<sub>RHE</sub>),<sup>36</sup> and under which the oxidation of urea<sup>37,38</sup> or ammonia<sup>27</sup> to NO<sub>3</sub><sup>-</sup>, NO<sub>2</sub><sup>-</sup>, or N<sub>2</sub> has previously been associated with the Ni(OH)<sub>2</sub> to NiOOH transformation. Nevertheless, the dominance of ammonia suggests that it is comparatively stable under these



conditions, preferentially remaining in the electrolyte rather than undergoing further oxidative conversion to  $\text{NO}_2^-$  and  $\text{NO}_3^-$ .

Ammonia formation was found to increase linearly over the 2 h electrolysis at 2.00  $V_{\text{RHE}}$  as a function of charge passed (**Figure 1c**). The assignment of ammonia as a glycine-derived product was further corroborated by isotope-labelling experiments using commercially available  $^{15}\text{N}$ -glycine, which showed a quantitative agreement in the ammonia production relative to experiments with unlabeled glycine (**Figure S23-S24**). However, alongside abundant  $^{15}\text{NH}_3$ , a non-negligible fraction of  $^{14}\text{NH}_3$  was also detected, which suggests isotopic or nitrogen impurities in the commercial  $^{15}\text{N}$ -labeled glycine, highlighting the need for caution when employing  $^{15}\text{N}$ -labeled glycine in mechanistic studies of nitrogen-containing products.

The increase in ammonia was accompanied linearly with significant  $\text{Ni}^{2+}$  dissolution. The  $\text{Ni}^{2+}$  concentration in the electrolyte, quantified by ICP after the 2 h of electrolysis, reached up to  $\sim 120 \mu\text{mol}$ , which is substantially larger than the  $\sim 25\text{-}30 \mu\text{mol}$  of ammonia produced, indicative of  $\sim 2\text{-}5\text{x}$  more Ni dissolved than ammonia formed. While all three institutions encountered challenges in reliably quantifying dissolved Ni (**Figure S25-S26**), the  $\text{Ni}^{2+}$  values shown in **Figure 1c** were quantified with confidence (see **Supplementary Note 3**) and represented the upper bound across trials. Notably, the Ni dissolution without glycine was found to be negligible ( $< 0.1 \mu\text{mol}$  in 0.1 M KOH electrolyte at 2.00  $V_{\text{RHE}}$  over 2 hours, see **Figure S27**). The glycine-promoted Ni dissolution can be attributed to the exothermic complexation of Ni(II) with glycinate (the deprotonated form of glycine), for which the aqueous complexation enthalpy at 25 °C has been reported as  $-36.7 \text{ kJ mol}^{-1}$ .<sup>39</sup> Notably, the coupled ammonia production and Ni dissolution could point to a dissolution-mediated pathway for ammonia formation, wherein Ni-ammonia complexation lowers the thermodynamic and/or kinetic barrier of making ammonia. For example, the formation of Ni-NH<sub>3</sub> complex (i.e.  $\text{Ni}^{2+} + 6\text{NH}_3 \rightarrow [\text{Ni}(\text{NH}_3)_6]^{2+}$ ) has an overall reaction enthalpy of  $-94.6 \text{ kJ mol}^{-1}$  at 25 °C according to DFT computation,<sup>40</sup> indicating strong stabilization of coordinated ammonia, which can stabilize NH<sub>3</sub> in solution from further oxidation to  $\text{NO}_2^-$  or  $\text{NO}_3^-$  under the oxidative conditions used in this work. This will be discussed further in the screening of other amino acids below. Further mechanistic studies are required to understand how glycine enhances Ni corrosion and whether soluble Ni species facilitate ammonia production under oxidative conditions. Interestingly, prior electrochemical studies on real waste activated sludge



under pulsed electrolysis conditions (1.35 V vs Hg/HgO, 0.2 M NaOH, 2 h) did not report significant Ni dissolution,<sup>12</sup> suggesting that the complex matrix of real sludge comprising proteins, polysaccharides, lipids, and extracellular polymeric substances may provide passivation or competitive complexation that protects the Ni surface. The particularly strong complexation of Ni(II) with glycinate may be uniquely aggressive compared to the diverse ligand environment present in real sludge, with important implications for catalyst design: electrode alloys or surface modifications that reduce glycinate complexation may improve stability during amino acid electrolysis. Overall, the high anodic overpotential and Ni instability raise concerns regarding the practical viability of ammonia recovery from amino acids on Ni. Further assessment of electrode stability under continuous operation in more practical setups (e.g., flow cells), as well as understanding and mitigating surface passivation in real sludge, will be important directions for future work.

The ammonia faradaic efficiency became larger when the working electrode potential was increased from 1.60 to 2.05 V<sub>RHE</sub>, and then decreased at further increasing potentials (**Figure 1d** and **Figure S28**). The Faradaic efficiency of ammonia, calculated using equation (2) with  $z_e = 6$  assuming full oxidation of carbon to CO<sub>2</sub> as an upper bound of efficiency (**Table 2**), increased from ~10% to ~38%, where the latter was operated at a higher potential than the 2.00 V<sub>RHE</sub> benchmarking condition, which corresponds to 2.05 V<sub>RHE</sub> after iR-correction. The logarithm of the ammonia formation rate was found to be proportional to the applied potential between 1.60 V<sub>RHE</sub> and 2.05 V<sub>RHE</sub>, with a Tafel slope of  $277 \pm 22$  mV dec<sup>-1</sup> (**Figure S5**). This behavior suggests that ammonia formation is governed either by an electrochemical rate-determining step or by a chemical rate-determining step involving electrochemically-generated active sites. It is noted that the potential ( $\geq 1.60$  V<sub>RHE</sub>) needed to produce ammonia (**Figure 1d**, **Figure S5**) is significantly more positive than the standard thermodynamic potential of glycine oxidation to make ammonia,  $\text{NH}_2\text{CH}_2\text{COOH}_{(s)} + 2\text{H}_2\text{O}_{(l)} \rightarrow 2\text{CO}_2 + \text{NH}_3 + 6\text{H}^+ + 6\text{e}^-$ ,  $E^0 = +0.06$  V<sub>RHE</sub> (see **Table S2** for details), indicative of slow kinetics for ammonia production. Nevertheless, Ni foil exhibited a considerably lower oxidative overpotential than Au and Pt, where ammonia production became apparent only at potentials  $>2.1$  V<sub>RHE</sub> and  $>2.6$  V<sub>RHE</sub>, respectively (**Figure S5**), signifying the surface-dependence glycine conversion to ammonia. For Ni, the decrease in ammonia FE upon further increase in the potential beyond 2.05 V<sub>RHE</sub> is not understood. We hypothesize that this may occur due to competing processes such as O<sub>2</sub> evolution and Ni corrosion, and/or lower activity



toward glycine oxidation on further oxidized Ni surfaces<sup>41</sup> (e.g. NiO<sub>2</sub>). On the other hand, reduction at constant potentials such as -0.4 V<sub>RHE</sub> and below did not show any ammonia production (**Figure S28**), suggesting the role of oxidation in glycine activation, nitrogen liberation and ammonia formation. At the benchmarking condition (representative data shown in the right panel of **Figure 1d**), the three institutions consistently reported an ammonia FE of 23.5 ± 2.2%, where the uncertainty was attributed to experimental factors such as variations in the *iR-corrected* potential across trials and electrode and electrolyte preparations (e.g. dilution errors). The Faradaic efficiency toward NO<sub>2</sub><sup>-</sup>/NO<sub>3</sub><sup>-</sup> collectively accounted for comparable percentages of ~25%. A significant portion of charge (on average ~10%) was associated with Ni corrosion while the remaining charge (~40%) was attributed O<sub>2</sub> evolution, thereby closing the charge balance. Overall, these benchmarking efforts, which are focused on uncovering the faradaic efficiency and distribution of N products and Ni dissolution, demonstrated consistent cross-institution alignment in capturing the experimental findings of glycine oxidation on Ni. Next, a more detailed understanding of glycine transformation was investigated through multi-technique carbon detection to enable the elucidation of possible reaction pathways during glycine oxidation.



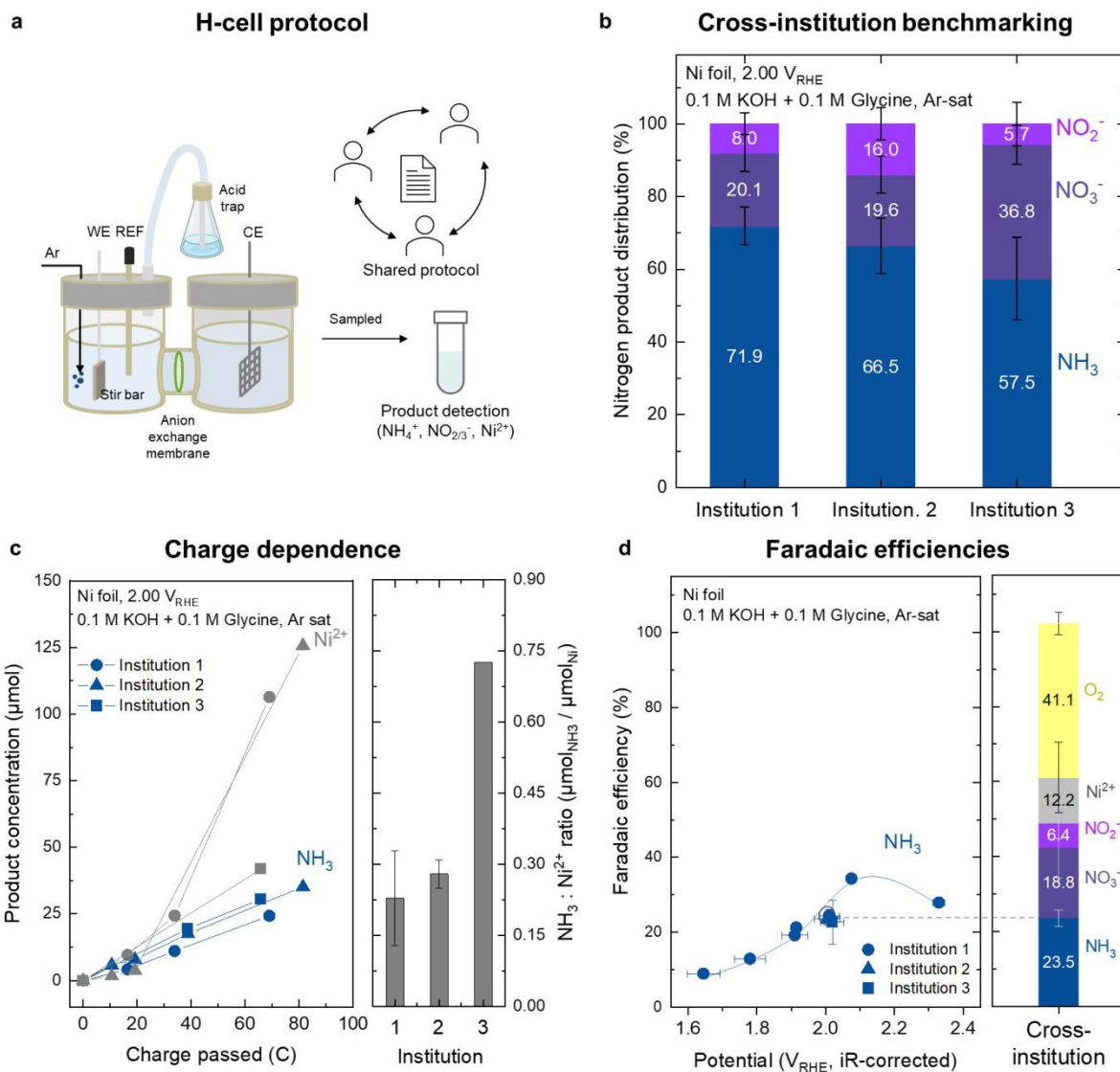
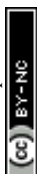


**Figure 1. Experimental benchmarking of electrochemical glycine oxidation on Ni.** **a)** H-cell setup for electrochemical glycine oxidation with Ni foil at 2.00 V<sub>RHE</sub> 0.1 M KOH + 0.1M glycine (Ar-sat). **b)** cross-institution benchmarking of nitrogen products in the electrolyte, showing ammonia-dominated nitrogen product. Error bars indicate n≥3 repeats (**Figure S17**). It is noted that the benchmarking condition for Institution 3 corresponds to no stirring condition, which is more similar to data from institution 1 and 2 using a small stir bar (10 mm at 300 rpm). More discussion can be found in relation to **Figure 4**. **c)** Time-dependent profile of ammonia (blue, measured via Ion chromatography or H-NMR) and Ni corrosion (gray, measured via ICP-MS) with respected to cumulative charge passed on Ni foil at 2.00 V<sub>RHE</sub>, showing significant electrode dissolution alongside ammonia generation. **d)** Potential-dependent faradaic efficiency to ammonia, calculated assuming z<sub>e</sub>=6 from NH<sub>2</sub>CH<sub>2</sub>COOH + 2H<sub>2</sub>O<sub>(l)</sub> → NH<sub>3(g)</sub> + 2CO<sub>2(g)</sub> + 6(H<sup>+</sup> + e<sup>-</sup>), see **Table 2**. The Faradaic efficiency at 2.00 V<sub>RHE</sub> corresponds to the benchmarking condition over 2 h electrolysis, while the faradaic efficiencies at other potentials were obtained from the potential screening experiment where 15-min chronoamperometry holds (CA) were conducted over time in the same electrolyte (see **Figure S4**). The right panel shows cross-institution cumulative faradaic efficiency for the different



products, assuming  $z_e=15, 14, 2$  and  $4$  for  $\text{NH}_2\text{CH}_2\text{COOH}/\text{NO}_3^-,\text{CO}_2$ ;  $\text{NH}_2\text{CH}_2\text{COOH}/\text{NO}_2,\text{CO}_2$ ,  $\text{Ni}/\text{Ni}^{2+}$  and  $\text{OH}^-/\text{O}_2$  respectively. Details of faradaic efficiency calculation can be found in **Table 2**.

### Carbon product characterization

Multiple characterization techniques of the post-electrolysis solutions revealed a diversity of carbon products resulting from electrochemical glycine oxidation. Following the reproducible nitrogen product characterization across the three institutions (**Figure 1**), the post-electrolysis electrolytes at  $2.00 \text{ V}_{\text{RHE}}$  were independently analyzed for carbon-containing species. Based on HPLC analysis performed by Institution 2, two dominant peaks at retention times of 18.5 min and 20.8 min systematically increased with electrolysis time, which were attributed to glycolic acid and formic acid, respectively, based on comparison with standard spectra (**Figure 2a**). Minor peaks at 14.2 min indicated the presence of glyoxylic acid while other minor peaks at 16.4 min, 19.6 min, and 21.8 min could not be assigned, indicative of other carbon products. In addition, anion chromatography using KOH gradient elution developed specifically for this detection confirmed the formation of formate (**Figure 2b**), consistent with the HPLC observations. Notably, anion chromatography showed the glyoxylate peak at a retention time of 4.4 min greater than that of glycolate at 12.1 min, opposite to that observed by HPLC, which might be due to subtle differences in mass transport not captured in the benchmarking protocol across institutions (see discussion of **Figure 4** below). Moreover, Institution 1 employed  $^{13}\text{C}$  NMR spectroscopy after performing the electrolysis with  $^{13}\text{C}_2$ -glycine (both carbon atoms isotope-labeled), which showed a prominent resonance at  $\sim 165$  ppm, attributable to carbonate ( $^{13}\text{CO}_3^{2-}$ )<sup>42</sup> that came from the dissolution of  $\text{CO}_2$  in the basic solution (pH=10.7 measured for the 0.1 M KOH + 0.1 M glycine electrolyte). To assess the carbon balance,  $\text{CO}_3^{2-}$  quantification via electrolyte acidification post-electrolysis showed that it represented 80% of the consumed glycine (**Figure S32**), thus validating the assumption that the carbon undergoes full oxidation to  $\text{CO}_2$  under the harsh oxidative condition in this work. An NMR peak at  $\sim 123$  ppm (**Figure 2c**) revealed the presence of cyanide ( $\text{CN}^-$ )<sup>43</sup>, which is independently verified by Institution 3 via colorimetric methods (see **Experimental Section**). Furthermore, several minor NMR peaks were observed: formaldehyde at  $\sim 82$  ppm<sup>44</sup> and glyoxylate at  $\sim 90$  ppm,<sup>45</sup> in agreement with HPLC and anion chromatography results (**Figure 2a-b**). Formate, although identified as a dominant product by HPLC and ion chromatography, could not be unambiguously resolved by  $^{13}\text{C}$  NMR due to overlap with the carboxylate carbon of glycine. The ammonia Faradaic efficiency from electrolysis with  $^{13}\text{C}_2$  quantitatively matched that with



unlabeled glycine, confirming that reproducible conditions were achieved during the product analysis (**Figure S25**). Overall, the combined carbon product analyses revealed a diverse set of glycine oxidation products at 2.00 V<sub>RHE</sub> on Ni, including predominantly formate, glyoxylate, glycolate, formaldehyde, cyanide, and CO<sub>2</sub> in the form of CO<sub>3</sub><sup>2-</sup>. Identification of these carbon products provides important constraints on the reaction pathways by which glycine is transformed to ammonia.

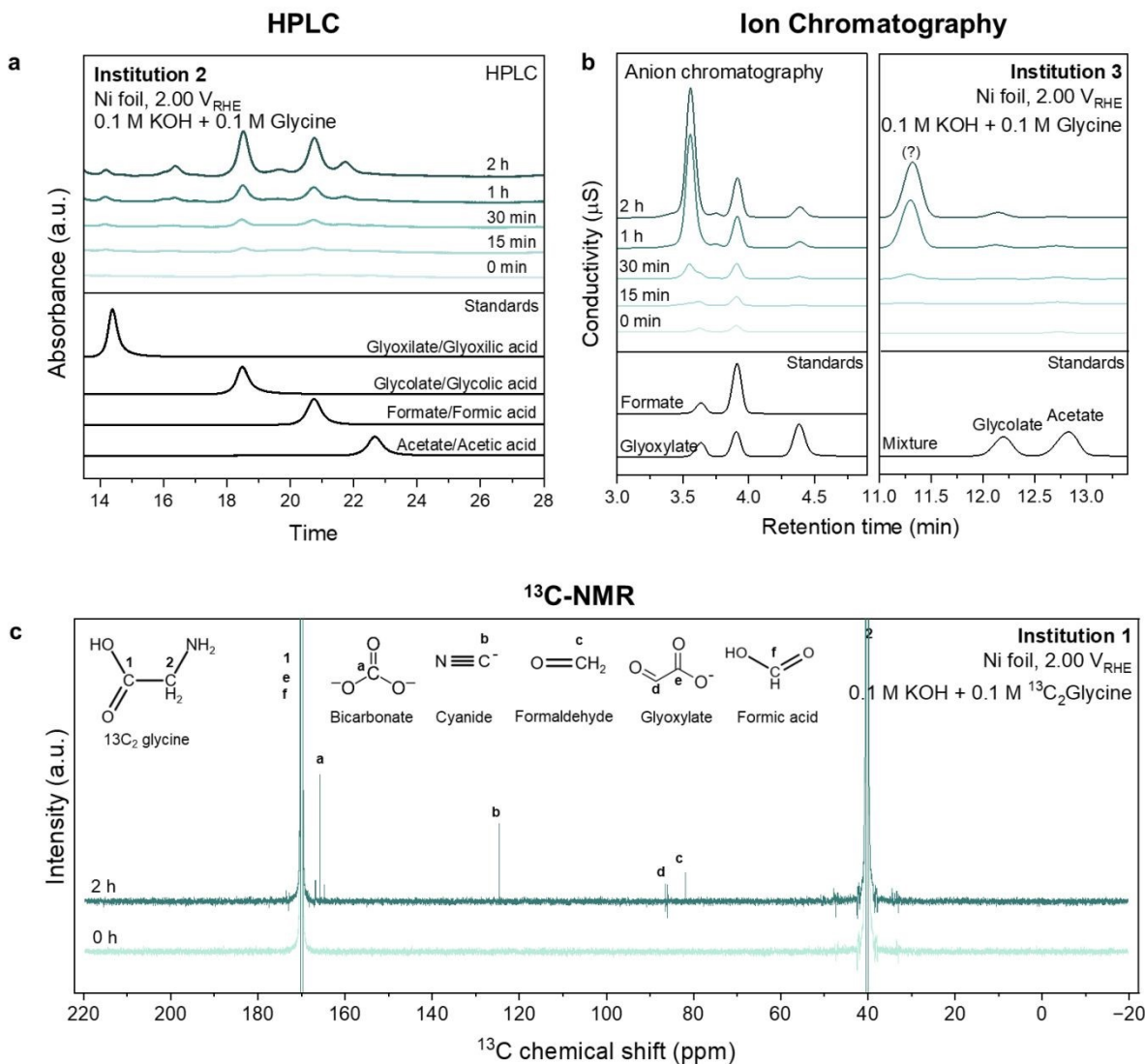


**Figure 2. Characterization of carbon byproducts** during electrochemical glycine oxidation on Ni at 2.00 V<sub>RHE</sub>. a) HPLC of electrolyte solutions at increasing reaction time up to 2 h. Carbon product standards are shown in the lower panel. b) Anion chromatography spectra of electrolyte solutions undergoing electrochemical glycine oxidation at increasing time stamps up to 2 h. The glycolate-acetate detection (right panel) has been specifically conducted at a higher column temperature to separate these peaks, which would



otherwise overlap at room temperature (see **Supplementary Information**). c)  $^{13}\text{C}$ -NMR spectra of glycine electro-oxidation using  $^{13}\text{C}_2$  glycine, where products such as carbonate, cyanide, formaldehyde, glyoxylate and formic acid appeared after 2 h of electrolysis. The experimental condition corresponds to the benchmarking condition of Ni electrode at 2.00  $V_{\text{RHE}}$  as described in **Figure 1**.

### Reaction pathways of electrochemical glycine oxidation

The diverse experimentally detected carbon byproducts suggests that multiple reaction pathways are operative during electrochemical glycine oxidation at 2.00  $V_{\text{RHE}}$  (**Figure 3a**). The detection of an N-containing  $\text{C}_1$  intermediate (i.e.,  $\text{CN}^-$ ) implies that the initial step of glycine activation may involve direct C–C bond cleavage, consistent with pathway 1 (**Figure 3a**, top). Through this pathway, glycine could be converted to methylamine ( $\text{CH}_3\text{NH}_2$ ), which may subsequently transform into formaldehyde and ammonia via a  $\text{CN}^-$  intermediate. This intermediate is supported by previous in-situ spectroscopy studies, where surface-bound  $^*\text{CN}^-$  and  $^*\text{CNO}^-$  were identified on  $\text{Pt}^{24}$  and  $\text{Au}^{25}$  based on the peak location and the stark shifts. However, the direct C–C bond cleavage in glycine necessary to form methylamine requires a two-electron reduction of glycinate (the deprotonated form of glycine) via  $\text{NH}_2\text{CH}_2\text{COO}^- + 2\text{OH}^- + 2e^- \rightarrow \text{CH}_3\text{NH}_2 + 2\text{H}_2\text{O} + \text{HCOO}^-$ , which may be unfavorable under strongly oxidative conditions. Nevertheless, methyl-, dimethyl-, and trimethylamine have been detected in previous work, including during electrolytic oxidation of  $\alpha$ -amino acids in acid on  $\text{PbO}_2$  by Takayama *et al.*<sup>21</sup> and during glycine oxidation at pH 13 on Pt reported by Maragoni *et al.*,<sup>21</sup> suggesting that the formation of methylamine can occur despite oxidizing electrode potentials, potentially via coupled oxidation-reduction processes. Methylamine, which would lead to  $\text{CH}_4\text{N}^+$  fragments at  $m/z = 30$  was not detected in this work (**Figure S18**), potentially due to its fast conversion to other products, including  $\text{CN}^-$ , which was detected as a prominent reaction product (**Figure 2c**) from oxidative transformation of methylamine to  $\text{CN}^-$ . Once formed,  $\text{CN}^-$ , being hydrogen-deficient, could undergo further oxidation to cyanate ( $\text{CNO}^-$ ), nitrite  $\text{NO}_2^-$ , and nitrate  $\text{NO}_3^-$  which has been reported to occur electrochemically on a copper-complex at 0.75 V vs Hg/HgO at pH = 12 ( $\sim 1.5 V_{\text{RHE}}$ ),<sup>46</sup> suggesting  $\text{CN}^-$  as a selectivity marker favoring  $\text{NO}_x$  formation over  $\text{NH}_3$ . Alternatively, sequential protonation of nitrogen coupled with C–N bond cleavage could lead to ammonia formation  $\text{CN}^- + \text{OH}^- + \text{H}_2\text{O} \rightarrow \text{NH}_3 + 2e^- + \text{CO}_2$ , consistent with prior reports of ammonia production from cyanide using Ti/ $\text{SnO}_2$ -based anodes.<sup>47</sup> Further studies are needed to elucidate the electrochemical oxidation of  $\text{CN}^-$  to form  $\text{NH}_3$  vs.  $\text{NO}_x$ .



Alternatively, the existence of C<sub>2</sub> products without containing nitrogen, such as glyoxylate (OCH-COO<sup>-</sup>) and glycolate (HOCH<sub>2</sub>COO<sup>-</sup>) suggests that direct C-N bond cleavage to liberate ammonia could occur on Ni, as depicted in Pathway 2 (**Figure 3**, bottom). In this route, glycine is oxidized directly to glyoxylate (OCH-COO<sup>-</sup>) and ammonia according to  $\text{NH}_2\text{CH}_2\text{COO}^- + 2\text{OH}^- \rightarrow \text{OCH-COO}^- + \text{NH}_3 + \text{H}_2\text{O} + 2\text{e}^-$  and the carbon in glyoxylate gets further oxidized to formate and ultimately CO<sub>2</sub>. Interestingly, glycolate likely comes from two-electron reduction of glyoxylate, which is commonly observed in biological systems through glyoxylic acid reductase (GAR).<sup>48</sup> Thus, its presence at 2.00 V<sub>RHE</sub> may imply a coupled oxidation-reduction process occurring on Ni, which warrants further investigation. Overall, glycine activation via either C-C cleavage (Pathway 1) or C-N cleavage (Pathway 2) appears to be feasible during electrochemical oxidation on Ni, but the extent of the two pathways requires considerations of the reaction energetics.

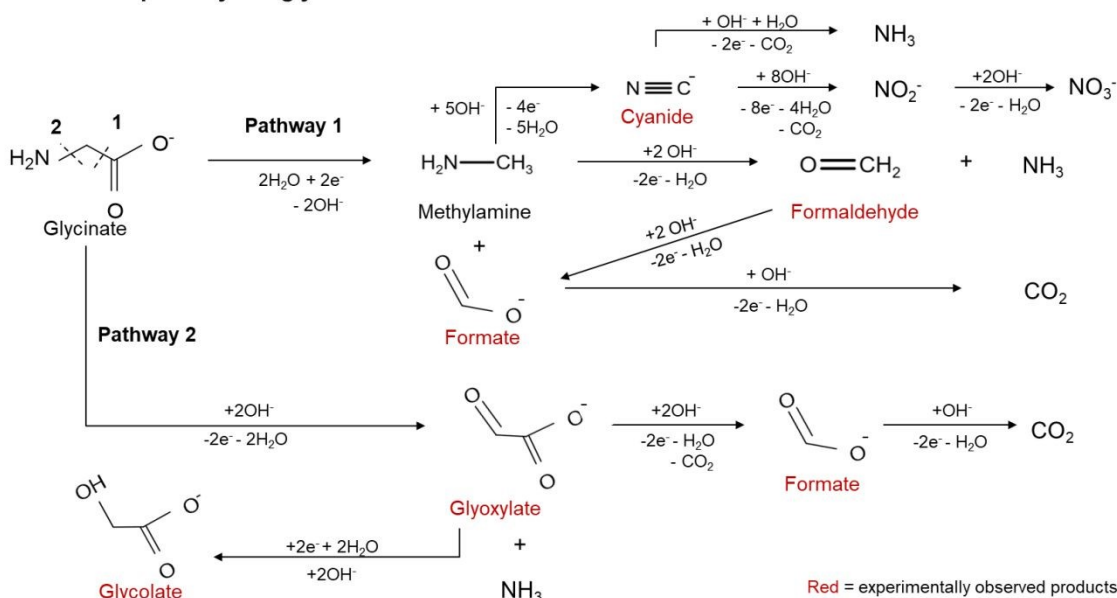
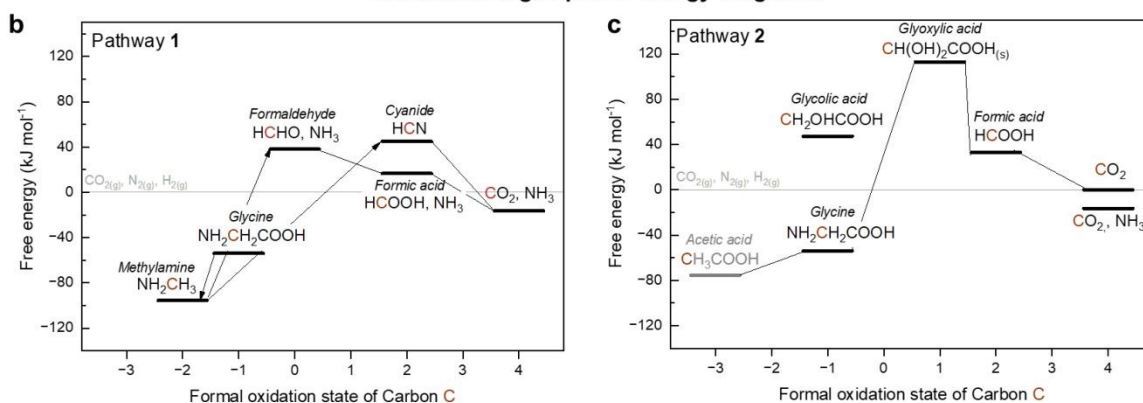
We further discuss the feasibility of different mechanisms by examining the thermodynamic stability of the reaction intermediates using the gas or solution phase free energies (**Figure 3 b-c**). We note that the bulk thermodynamic values do not include surface adsorption or electric field effects prominent in electrochemical reactions on a heterogenous surface, but can provide a starting point in understanding the relative stability of reaction intermediates. Such thermodynamic analysis indicates that both pathways involve a similarly uphill step, and that C-N bond cleavage is generally the most energetically uphill step. Using standard Gibbs formation energies for carbon-containing species (**Table S3**), the energy diagram for Pathway 1 (**Figure 3b**) shows that the conversion of methylamine to formaldehyde and ammonia  $\text{CH}_3\text{NH}_{2(\text{g})} + 2\text{OH}^- \rightarrow \text{CH}_2\text{O}_{(\text{g})} + \text{NH}_{3(\text{g})} + 2\text{e}^- + \text{H}_2\text{O}_{(\text{l})}$  is the most uphill step, with  $\Delta G_r = +150.0 \text{ kJ mol}^{-1}$ . The subsequent oxidation of formaldehyde to formic acid and CO<sub>2</sub> is energetically downhill. When cyanide is considered as an intermediate, its formation from methylamine  $\text{CH}_3\text{NH}_{2(\text{g})} + 5\text{OH}^- \rightarrow \text{HCN}_{(\text{l})} + 2\text{e}^- + \text{H}_2\text{O}_{(\text{l})}$  is the most uphill step ( $\Delta G_r = 140.5 \text{ kJ mol}^{-1}$ ), while further oxidation to NH<sub>3</sub> and CO<sub>2</sub> is thermodynamically favorable. The experimental observation of CN<sup>-</sup> as a prominent byproduct is at odds with the thermodynamic analysis, indicating that kinetic barriers on the surface or other surface thermodynamic reaction steps should be considered. For Pathway 2 (**Figure 3c**) involving sequential oxidation of glycine to glyoxylic acid, formic acid, and CO<sub>2</sub>, glycine oxidation to glycolic acid via  $\text{NH}_2\text{CH}_2\text{COOH}_{(\text{s})} + 2\text{H}_2\text{O}_{(\text{l})} \rightarrow \text{CH}(\text{OH})_2\text{COOH} + \text{NH}_3 + 2\text{H}^+ + 2\text{e}^-$ ,  $\Delta G_r = +150.4 \text{ kJ mol}^{-1}$ , is the most uphill step. The subsequent oxidation steps of carbon from glyoxylic acid to ultimately CO<sub>2</sub> appeared to be strongly downhill. This analysis supports C-N bond cleavage as the



rate-determining step. However, capturing the true rate-limiting steps and reaction selectivity will require a detailed investigation of charged species adsorption (e.g., glycinate/carboxylate species and  $\text{CN}^-$ ). This will involve grand-canonical density functional theory and microkinetic modeling, supported by experimental probes such as kinetic isotope effects and Tafel slope analysis, and is the subject of future work.

We consider several hypotheses regarding the origin of the oxidizing species responsible for glycine oxidation on the Ni surface. One possibility is oxidation mediated by NiOOH formed through the  $\text{Ni}^{2+}/\text{Ni}^{3+}$  redox transition,<sup>49,50</sup> described by  $\text{Ni}(\text{OH})_{2(\text{s})} + \text{OH}^-_{(\text{aq})} \rightarrow \text{NiOOH}_{(\text{s})} + \text{H}_2\text{O}_{(\text{l})} + \text{e}^-$ . NiOOH can therefore act as a primary oxidant, which has been demonstrated for the electrochemical oxidation of urea<sup>27,37</sup> and alcohols.<sup>28</sup> This hypothesis is supported by the fact that glycine oxidation to ammonia occurs at potentials  $>1.60 V_{\text{RHE}}$  (**Figure 1d**), which are well-above the  $\text{Ni}^{2+}/\text{Ni}^{3+}$  redox transition at  $\sim 1.35 V_{\text{RHE}}$ .<sup>51</sup> Alternatively, the formation of surface  $\text{NiO}_x$  species may enable the generation of reactive oxygen species such as peroxide and superoxide species, with prior studies indicating that hydroperoxides<sup>52</sup> and  $\text{OH}\cdot$  radical,<sup>53</sup> such as those generated via Fenton chemistry, can oxidize amino acids. Another possibility involves singlet oxygen ( $^1\text{O}_2$ ), a highly reactive oxidant that can arise from spin-conservation constraints during oxygen evolution and then decay to triplet oxygen ( $^3\text{O}_2$ ). The generation of  $^1\text{O}_2$  has been reported on Ni-based cathodes,<sup>54</sup> where it induces severe oxidative decomposition of aprotic solvents to generate carbon-byproducts such as Li-acetate, Li-formate and  $\text{Li}_2\text{CO}_3$  that severely limit cyclability of Li-ion and Li- $\text{O}_2$  batteries,<sup>54</sup> and is thermodynamically accessible with a calculated reversible potential of  $1.475 V_{\text{RHE}}$  for  $2\text{H}_2\text{O} \rightarrow ^1\text{O}_2 + 4\text{H}^+ + 4\text{e}^-$ .<sup>55</sup> Interestingly, these aprotic byproducts are structurally similar to glycinate (structurally equivalent to acetate but with an  $-\text{NH}_2$  group substituted onto the methyl carbon), formate and  $\text{CO}_3^{2-}$  detected in this work (**Figure 2**), hinting at  $^1\text{O}_2$  as a possible oxidant assuming similar reactivity in protic environments. Further mechanistic studies are therefore required to identify the dominant oxidizing species responsible for glycine activation, which will inform future catalyst design aimed at decoupling oxidant generation from electrode corrosion.



**a Reaction pathways of glycine oxidation****Solution and gas phase energy diagrams**

**Figure 3. Reaction pathways during electrochemical glycine oxidation.** a) Proposed reaction pathways based on the detected reaction products, denoted in red as characterized in **Figure 2**. Free energy diagrams of the pure phases with increasing oxidation state of the carbon are depicted for pathway 1 (**b**) and pathway 2 (**c**) based on the available thermodynamic data. All species and reactions are expressed in their protonated form and used the standard free energy of formation of the pure phases: crystalline solids for glycine, glyoxylic acid (i.e. in its hydrated form, dihydroxyacetic acid) and glycolic acid; liquids for acetic acid, formic acid, cyanic acid (HCN); gases for formaldehyde, methylamine, CO<sub>2</sub>, NH<sub>3</sub> and H<sub>2</sub>. Formal oxidation states were assigned using the ionic approximation by attributing bonding electrons to the more electronegative atom, and the resulting charge defines the oxidation state. Zero free energy corresponds to CO<sub>2(g)</sub>, NH<sub>3(g)</sub>, H<sub>2(g)</sub> at 1 bar and 298 K. Full chemical equations and the reaction free energy calculations can be found in **Table S3**.



### Assessing the influence of experimental conditions on product selectivity

Given the diversity of reaction products from glycine oxidation and motivated by the challenges in benchmarking the nitrogen selectivity across institutions (**Figure 1**), we investigated the effect of several experimental parameters such stirring, electrode area size and cell design (**Figure 4**). In addition to N selectivity, their influence on the selectivity to carbon byproducts are also particularly discussed to allow interpretation of mechanistic implications. At Institution 3, the benchmarking condition that yielded an ammonia Faradaic efficiency of  $\sim 26\%$  corresponded to a relatively static electrolyte without stirring, which more closely resembled the conditions at Institutions 1 and 2, where a small (10 mm) stir bar was used. The overall FE to these carbon byproducts amounted to 6% (**Figure 4**, bottom), which represents  $\sim 20\%$  of the carbon balance while the remaining  $\sim 80\%$  was attributed to  $\text{CO}_2$  (**Figure S33**). Institution 3 first conducted electrolysis using a larger 30 mm magnetic stir bar operating at 500 rpm. Increased convection led to a pronounced decrease in ammonia Faradaic efficiency from 26.8% to 17.5%. Faradaic efficiencies toward  $\text{NO}_2^-$  and  $\text{NO}_3^-$  also slightly decreased under stirring, with their combined contribution decreasing from  $\sim 32\%$  under static conditions to  $\sim 27\%$ , while the relative proportion of  $\text{NO}_2^-$  increased with stronger convection. Accordingly, the higher  $\text{NO}_2^-$  observed at Institutions 1 and 2 ( $\sim 10\text{-}16\%$ ) compared to Institution 3 during benchmarking (**Figure 1b**) may be attributed to an intermediate degree of convection (1.0 mm stir bar at 300 rpm), lying between static and strongly convective conditions explored at Institution 3 (**Figure 4a**, first two columns). Taken together, these observations suggest several mechanistic implications: First, although increased convection would be expected to reduce ammonia residence time near the electrode surface and suppress its further oxidation, ammonia Faradaic efficiency decreased without a corresponding increase in  $\text{NO}_2^-/\text{NO}_3^-$ , indicating that oxidized nitrogen species likely originate from direct amine oxidation rather than the oxidation of produced ammonia. Second, the enhanced formation of glyoxylate under larger convection (FE = 12.8% vs 3.4%), concurrent with suppressed ammonia and formate production, suggests that glycine activation via C-N cleavage (Pathway 2, **Figure 3a**) was favored by larger convection but less effective at producing ammonia than Pathway 1, in which ammonia and formate are generated via a methylamine intermediate (**Figure 3a**). Future work is needed to quantitatively resolve the influence of mass transport on product selectivity.



The effect of electrode surface area was investigated by doubling the electrode area while keeping the same electrolyte volumes in both compartments (i.e. 0.05 to 0.1 cm<sup>2</sup><sub>geo</sub>: mL ratio), with no stirring. Increasing the electrode area led to a substantial enhancement in ammonia Faradaic efficiency, from ~26% to ~40% (**Figure 4, top**). In contrast, the Faradaic efficiency toward NO<sub>3</sub><sup>-</sup> decreased markedly from 31.5% to 11.2% with the larger electrode. The carbon product distribution also exhibited discernible changes, with glycolate Faradaic efficiency increasing to 2.7% for the larger electrode compared to 0.5% at benchmarking (**Figure 4, bottom**). Taken together, these results indicate that a larger electrode area favors ammonia production, potentially by enabling a greater extent of coupled oxidation-reduction processes at the electrode surface when the oxidative potential 2.00 V<sub>RHE</sub> was applied. In this context, both methylamine formation from glycine and glycolate formation from glyoxylate involve reductive steps (**Figure 3a**), which may benefit from increased electrode area. These findings also suggest that reactor design and optimization of mass transport will be critical in controlling the activity and selectivity of practical amino acid electrolysis. Finally, the influence of cell design was evaluated by comparing the H-cell configuration (i.e. the benchmarking condition) with single compartment/undivided cell, while keeping the electrode area-to-volume ratio (i.e. 0.05 cm<sup>2</sup><sub>geo</sub> : mL) the same without stirring. The undivided cell produced an overall Faradaic efficiency for nitrogen-containing products (NH<sub>3</sub>, NO<sub>3</sub><sup>-</sup>, NO<sub>2</sub><sup>-</sup> and CN<sup>-</sup>) of 66.1%, comparable to the benchmark H-cell value of 63.2%, but with a larger fraction of NO<sub>3</sub><sup>-</sup> relative to NH<sub>3</sub> (**Figure 4, top**). In addition, glycolate Faradaic efficiency increased to 3.3% from 0.5% in benchmarking condition (**Figure 4, bottom**). This shift in selectivity may be linked to the pH drop during electrolysis: during the benchmarking H-cell conditions with an anion-exchange membrane, the working electrode compartment experienced a larger pH drop ( $\Delta\text{pH} \approx -0.5$ ) compared to the undivided cell ( $\Delta\text{pH} \approx -0.2$ , see **Figure S34** and **Table S4**). These observations suggest that electrolyte pH may influence glycine oxidation pathways and the resulting ammonia and carbon product selectivity, warranting further investigation.



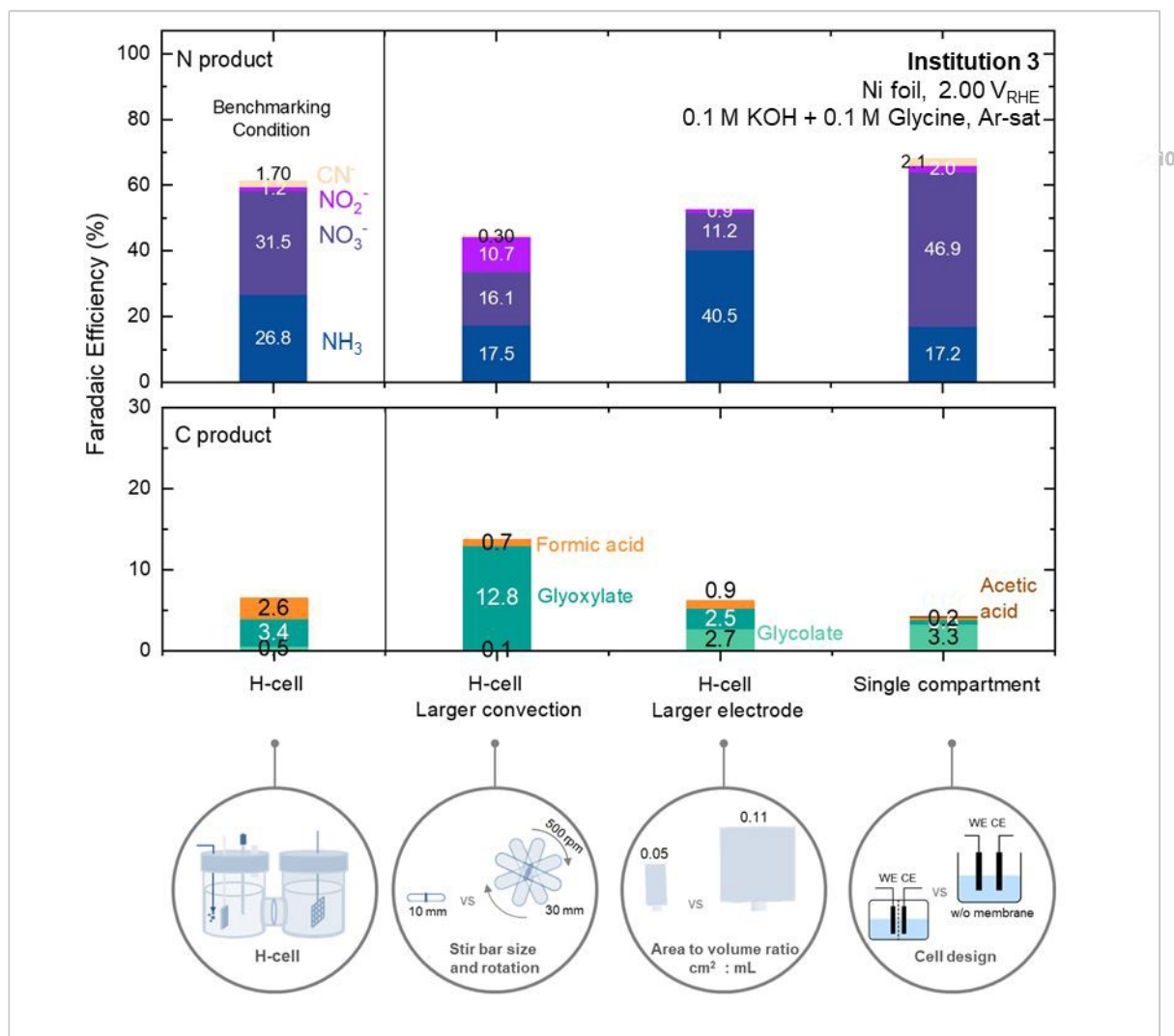


**Figure 4.** Effect of experimental design on the nitrogen and carbon products of electrochemical glycine oxidation on Ni. The benchmarking condition (most left) corresponds to conditions described in Figure 1, using an H-cell containing an anion-exchange membrane and micro stir bar (10 mm) rotated at 300 rpm. The faradaic efficiencies from experiment 3-1 from institution 3 has been plotted (see **Table S1**) as the carbon product quantification is available for this experiment. Relative to the benchmarking condition, three changes of experimental conditions have been investigated: larger convection via higher rotation of a larger stir bar, larger electrode area and undivided compartment (i.e. single cell) in lieu of H-cell, showing significant influence of these factors on the production and distribution of the N- (top panel) and C-based (bottom panel) products. The faradaic efficiency calculation for NH<sub>4</sub><sup>+</sup>, NO<sub>3</sub><sup>-</sup>, NO<sub>2</sub><sup>-</sup> and CN<sup>-</sup> and for glycolate, glyoxylate and formic acid can be found in **Experimental Section**.



## Impact of potential pulsing on ammonia efficiency

Recognizing the benefits of dynamic electrocatalysis via potential pulsing, the effects of pulsing are herein investigated, with particular emphasis on how the resulting Faradaic efficiencies differ from those obtained under constant potential. Three potential pulsing were investigated and compared to the ‘benchmarking’ constant potential experiment at 2.00  $V_{\text{RHE}}$  (**Figure 5a**). A symmetric 5 s hold at the positive and negative potentials was selected based on timescales over which pulsing effects have been reported in other electrochemical reactions,<sup>30,31</sup> providing a reasonable starting point. For Pulsing 1-3, progressively higher positive potentials were applied (**Figure 5b–d**). The raw negative potential (prior to iR correction) was kept constant and sufficiently negative ( $< -0.10 V_{\text{RHE}}$ ) to promote surface \*H coverage on Ni,<sup>56</sup> which may be important in facilitating hydrogenation of amine to ammonia. After iR correction, however, the negative potential varied within  $\pm \sim 20$  mV due to fluctuations in the recorded current (**Figure 5b–d**). Several observations emerge from the electrochemical profiles. First, the working electrode potentials after iR correction during pulsing showed considerably larger variations compared to constant-potential electrolysis. The stabilized positive potentials, obtained by averaging the final 1 s of each 5 s pulse (**Figure S38–S40**), were  $1.65 V_{\text{RHE}} \pm 7$  mV (**Figure 5b, e**)  $1.78 V_{\text{RHE}} \pm 7$  mV (**Figure 5c, f**) and  $1.83 V_{\text{RHE}} \pm 67$  mV (**Figure 5d, g**). However, when the whole 5s is considered (excluding the first 0.1 s from capacitive contributions), iR-corrected potential variation during the positive pulse increased to  $\sim 60$  mV,  $\sim 100$  mV and  $\sim 400$  mV for pulsing 1, 2 and 3 respectively (**Figure S35–S37**). Second, differences were observed in the current-time profiles. For Pulsing 1 and 2, the positive pulses showed the conventional behavior of a high initial current decaying to a steady state (**Figure 5e, f**), consistent with a transition from capacitive to faradaic currents. In contrast, Pulsing 3 exhibited a more rounded/unusual initial response (**Figure 5g, Figure S37**). Analysis of the raw (uncorrected) potential indicates that this arises from a longer time ( $\sim 0.5$  s) required for the potential to reach its set value (**Figure S40**), likely due to potentiostat overload at high potentials, which limits accurate capture of currents at the initial stages. These observations underscore the importance of improved cell designs with reduced solution resistance for accurate high-potential pulsing studies.

Ammonia Faradaic efficiency (FE) with pulsing generally shows a significant improvement relative to constant-potential electrolysis, yet the magnitude of this enhancement is



highly sensitive to how the Faradaic charge is accounted for (**Figure 5h**). The constant-potential experiment yielded an ammonia FE of  $18.4 \pm 0.9\%$  over 1 h across three independent repeats. Notably, the same experiments produced an FE of  $23.8 \pm 1.0\%$  over 2 h (**Table S1**), consistent with cross-institution benchmarking results (**Figure 1**), indicating higher efficiency at longer electrolysis times. In calculating the FE from pulsing experiments, three accounting methods were used to calculate total faradaic charge ( $Q_{\text{total}}$ ): (i) summing positive and negative charges with their signs preserved (**Figure 5h**, left), (ii) considering only the positive charge (**Figure 5h**, middle) and (iii) summing the absolute values of positive and negative charges (**Figure 5h**, right). When method (i) is considered, serving as the most ‘optimistic’ estimate of the Faradaic efficiency, Pulsing 1 and 2 yield substantially higher ammonia FEs of up to  $\sim 80\%$ . In contrast, when negative charge contributions are excluded or counted in absolute terms (methods ii and iii), the calculated FEs decrease markedly and converge toward those obtained under constant-potential conditions. The sensitivity of FE to charge accounting is most pronounced for Pulsing 1 (**Figure 5b, e**), where the total positive charge passed is the lowest in magnitude and at levels comparable to the negative charge (**Table S5**). In addition, the FE from pulsing experiments exhibit generally larger error bars, which we attribute to the greater variation of the working electrode potential associated with *iR*-correction. Despite these variations, the enhancement in FE relative to constant-potential electrolysis remains robust beyond experimental uncertainty. In particular, Pulsing 2, which employs a lower positive potential of  $1.78 V_{\text{RHE}} \pm 7 \text{ mV}$ , delivers at least  $\sim 10\%$  higher ammonia FE ( $\sim 30\%$  as the lower bound) than the static experiments at  $2.00 V_{\text{RHE}}$  (**Figure 5h, right**) regardless of the accounting methods used.

The enhancement in ammonia FE via pulsing suggests several mechanistic implications. The effectiveness in pulsing to the  $*\text{H}$  coverage regime ( $< -0.1 V_{\text{RHE}}$  on  $\text{Ni}^{56}$ ) implies that the rate-limiting step of C-N bond cleavage, which we hypothesized in accordance with the thermodynamic analyses in **Figure 3**, is linked to the hydrogenation of the amine group to form ammonia. At oxidative potentials, hydrogen availability is limited because water preferentially undergoes oxidation to  $\text{O}_2$  and  $\text{H}^+$  above  $1.23 V_{\text{RHE}}$ . Pulsing to negative potentials may therefore transiently increase  $*\text{H}$  coverage, facilitating amine hydrogenation and C-N bond cleavage. Alternatively, the benefit of pulsing may arise from active-site regeneration. In this case, cycling the potential enables repeated  $\text{Ni}^{2+}/\text{Ni}^{3+}$  redox transitions, regenerating  $\text{NiOOH}$  as the active oxidizing species and



sustaining the conversion. the sensitivity of pulsing results highlights the need for clear charge accounting and further mechanistic investigation to elucidate the contributions of positive and negative charge toward ammonia production. Nevertheless, they highlight opportunities to optimize pulsing conditions to enhance ammonia efficiency while reducing anodic overpotential, which should ultimately align with the upper-bound practical energy efficiency defined by future techno-economic analyses.



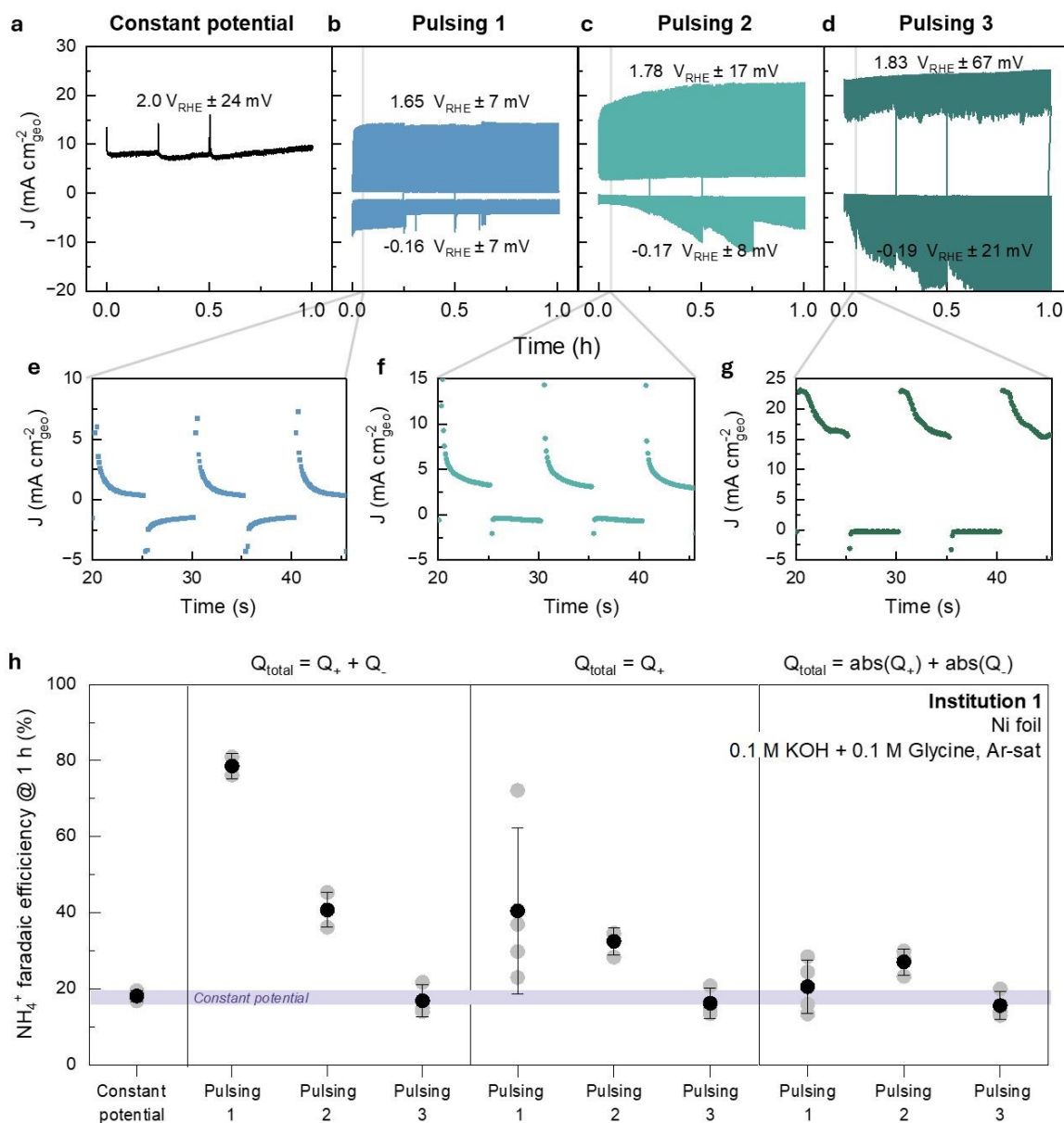


**Figure 5. Investigating the impact of potential pulsing on  $\text{NH}_4^+$  efficiency.** **a)** Chronoamperometry profile of electrochemical glycine oxidation with polished Ni at  $2.00 V_{\text{RHE}}$  0.1 M KOH + 0.1 M glycine (Ar-sat) over 1 hour, corresponding to the ‘benchmarking condition’ outlined in Figure 1. **b-d)** Electrochemistry profile of three pulsing conditions at increasing values of the positive potentials from  $+1.65 V_{\text{RHE}}$  (pulsing 1, **b**),  $1.78 V_{\text{RHE}}$  (pulsing 2, **c**) and  $1.83 V_{\text{RHE}}$  (pulsing 3, **d**), while the negative potential values are kept nominally similar but showed differences in currents resulting in differences in iR-corrected potentials. Zoomed-in view of the current profiles are shown in panels **e**, **f** and **g** for Pulsing 1, 2 and 3 respectively, where the positive and negative potentials were held for 5 s. The average and standard deviation of the potentials are determined from the last 1 s of the 5 s pulse (see **Figure S38-S40** for demonstration), during which the current is stable, over the entire 1 h duration and across 3 independent repeats. **h.**  $\text{NH}_4^+$  faradaic efficiency comparison between the constant potential experiments at  $2.0 V_{\text{RHE}}$  and the pulsing experiments with three different methods of charge accounting: the sum of positive and negative charges (left), the positive charges only (middle) and the absolute values of the positive and negative



charges. The faradaic efficiency to ammonia, calculated assuming  $z_e=6$  from  $\text{NH}_2\text{CH}_2\text{COOH} + 2\text{H}_2\text{O}_{(l)} \rightarrow \text{NH}_{3(g)} + 2\text{CO}_{2(g)} + 6(\text{H}^+ + \text{e}^-)$ , see **Table 2**. Error bars indicate  $n \geq 3$  independent measurements (see **Table S5-S6** for the tabulated results).



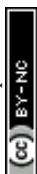
## Extending mechanistic insights to other amino acids

Given the diversity of amino acids and their compositions in activated waste sludge (see **Table 1**), we expand the electrochemical characterization to assess the applicability of insights derived from glycine to other amino acids. As an initial library, alanine, lysine, and aspartic acid were selected to represent a range of side groups: alanine with a simple methyl group at the  $\alpha$ -carbon, lysine with a side chain containing an additional amine, and aspartic acid with a carboxylic acid side group. Similar to glycine, electrochemical oxidation of these amino acids in alkaline electrolyte on Ni foil at 2.00 V<sub>RHE</sub> yielded NH<sub>3</sub> as the dominant nitrogen product (**Figure 6a**), accounting for 90%, 85%, and 85% of the total nitrogen for alanine, lysine, and aspartic acid, respectively. The remaining nitrogen balance is attributed to NO<sub>3</sub><sup>-</sup> and NO<sub>2</sub><sup>-</sup>, while no gas-phase nitrogen products such as N<sub>2</sub> and NO were detected (**Figure S41-43**). Similar to glycine, the production of the ammonia-dominated product is accompanied with appreciable Ni dissolution (**Figure S40**) albeit by different amounts, in the order of glycine (53.4  $\mu\text{mol} \pm 44.5$  over the 2 h electrolysis) > alanine (16.1  $\mu\text{mol}$ ) > lysine (0.1  $\mu\text{mol}$ ) > aspartic acid (0.1  $\mu\text{mol}$ ), which significantly exceeded that in the absence of amino acids (i.e. OER in 0.1 M KOH, **Figure S27**). Charge balance was assessed by computing the FE associated with the observed products (NH<sub>3</sub>, NO<sub>3</sub><sup>-</sup>, NO<sub>2</sub><sup>-</sup>, Ni<sup>2+</sup> and O<sub>2</sub>), assuming full oxidation of C to CO<sub>2</sub>. The ammonia FE follow a similar ranking in the order of alanine (FE<sub>NH3</sub> = 63.5% assuming  $z_{e^-} = 12$ ) > lysine (FE<sub>NH3</sub> = 45.4%,  $z_{e^-} = 14$ ) > glycine (FE<sub>NH3</sub> = 23.7%  $\pm 1.8$ ,  $z_{e^-} = 6$ ) > aspartic acid (FE<sub>NH3</sub> = 10.9%,  $z_{e^-} = 12$ , see **Table S1**). We note that the cumulative FE of glycine and aspartic acid including products from NH<sub>3</sub>, NO<sub>3</sub><sup>-</sup>, NO<sub>2</sub><sup>-</sup>, Ni dissolution and O<sub>2</sub> evolution reach 100% within experimental uncertainty (**Figure S44**), thereby closing the charge balance. On the other hand, those for alanine and lysine exceed unity by ~20%, which might suggest that the carbons were not fully oxidized to CO<sub>2</sub>, thereby resulting in the lower actual  $z_{e^-}$  values than  $z_{e^-} = 12$  and  $z_{e^-} = 14$ , respectively. Overall, screening of additional amino acids reveals a consistent trend of ammonia as the dominant nitrogen-containing product, accompanied by appreciable Ni dissolution. Meanwhile, variations in ammonia efficiency highlight the strong influence of side-chain character in governing amino acid oxidation.

We correlate ammonia production with competing processes and side-chain character to probe the mechanism of ammonia generation during amino acid oxidation. In lieu of FE, the product converted in moles normalized to the total charge passed (in units of mol of products per coulomb of passed charge,  $\mu\text{mol}_{\text{prod}} \text{C}^{-1}$ ), denoted as the charge efficiency to the product, has been



used to avoid ambiguity in the number of electrons  $z_e$ . Firstly, increasing charge efficiency toward ammonia was linearly correlated with decreasing charge efficiency to  $O_2$  (**Figure 6b**), indicating that  $O_2$  is parasitic to ammonia production. Mechanistically, this correlation supports the hypothesis that both processes share a common active site. In this context, NiOOH associated with the  $Ni^{2+}/Ni^{3+}$  transition is known to be key for  $O_2$  evolution activity<sup>51,57</sup> but may also competitively act as the primary oxidant for amino acid conversion to ammonia. Secondly, the charge efficiency to ammonia correlated approximately logarithmically with increased Ni dissolution (**Figure 6c**). This observation supports the hypothesis that dissolved Ni plays an active role in thermodynamically stabilizing ammonia, such as via the Ni-NH<sub>3</sub> complex. Another hypothesis consistent with this observation is that  $Ni^{2+}$  may kinetically accelerate amino acid decomposition via redox mediation: initial  $Ni^{2+}$ -amino acid complexation followed by oxidation to  $Ni^{3+}$  by the electrode generates a solution-phase oxidant that promotes oxidative deamination, releasing ammonia.<sup>58,59</sup> We further examine the relationship between  $Ni^{2+}$  dissolution and side-chain character. Previous computation<sup>60</sup> has shown that aspartic acid binds  $Ni^{2+}$  much more strongly ( $E_{\text{binding}} = \sim 350 \text{ kJ mol}^{-1}$ ) than other amino acids ( $E_{\text{binding}} = \sim 250 \text{ kJ mol}^{-1}$  for glycine, alanine and lysine) due to its two negatively charged carboxyl groups. However, the  $Ni^{2+}$  dissolution in aspartic acid ( $0.003 \text{ } \mu\text{mol}_{Ni} \text{ C}^{-1}$ ) is the lowest among the amino acids studied. This result suggests that the Ni electrode instability in the presence of amino acids stems not from the parasitic  $Ni^{2+}$ -amino acid coordination, but instead actively facilitates ammonia formation via nickel complexation, which improves the thermodynamic stability of ammonia and reaction intermediates and concurrently lowers kinetic barriers. Thirdly, increasing charge efficiency to ammonia is associated with increasing  $NO_{2/3}^-$  (**Figure 6d**). This result supports the hypothesis that  $NH_3$  and  $NO_{2/3}^-$  production are bottlenecked by a common rate-limiting step of C-N cleavage (see **Figure 4 b,c**). Based on these correlations, we hypothesize that the electrochemical activity for amino acid activation can be rationalized by the side-chain character (see top of **Figure 6**). (i) Glycine and alanine, with simple side groups, exhibit higher  $NH_3$  and  $NO_x$  efficiencies, likely due to higher surface coverage of amino acid adsorption. (ii) Lysine shows moderate efficiencies, where the longer side chain may reduce adsorption coverage despite the additional amine. (iii) Aspartic acid exhibits the lowest efficiencies, due to alternative COO<sup>-</sup>-down adsorption<sup>25</sup> on the positively charged Ni surface from the carboxylate side-group rather than the  $\alpha$ -functional group. While further work is needed to quantitatively link charge efficiency with broader amino acid



structures, these results provide insight into the origin of ammonia production and its dissolution-mediated mechanism under oxidative potentials.

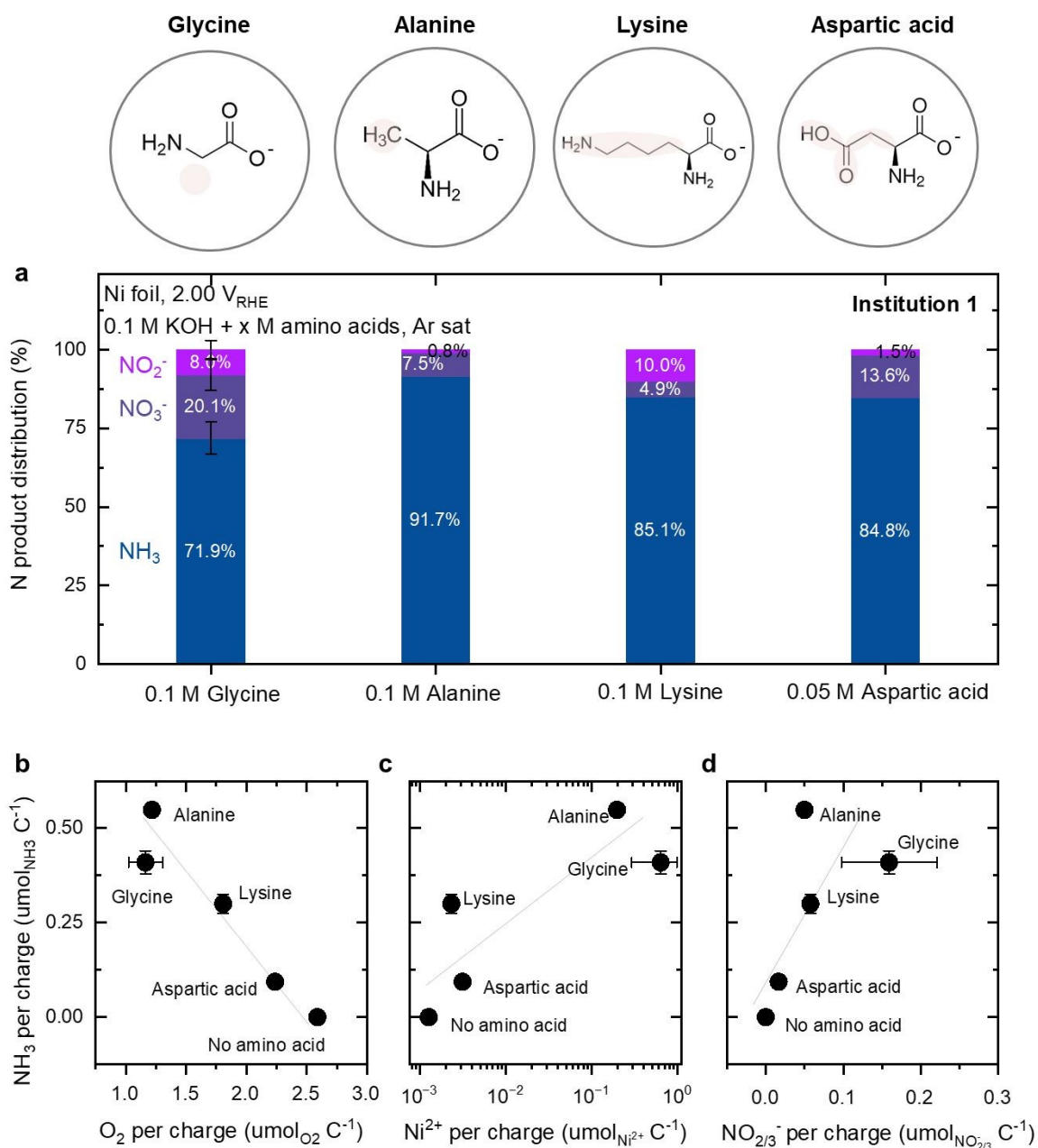


**Figure 6. Evaluating electrochemical oxidation of different amino acids.** a) Nitrogen product distribution ( $\text{NH}_3$ ,  $\text{NO}_3^-$  and  $\text{NO}_2^-$ ) from the electrochemical oxidation of glycine, alanine, lysine and aspartic acid in 0.1 M KOH with Ni foil in an H-cell. The molecular structures of the amino acids are displayed above. All experiments were conducted by Institution 1. The chronoamperometry profiles and quantification of gas and solution-phase products are shown in **Figure S41-43** and **Table S1**, respectively, where the average iR-corrected potentials over 2 hours were measured to be  $1.98 \pm 0.025 \text{ V}_{\text{RHE}}$ ,  $2.04 \pm 0.030$  and  $2.03 \pm 0.007$  for Alanine, Lysine and Aspartic acid respectively. b-d) Correlations between the



charge efficiency towards ammonia production and towards O<sub>2</sub> evolution (b), Ni dissolution (c) and NO<sub>2/3</sub><sup>-</sup> production (d). Data correspond to electrochemical oxidation of the four amino acids in alkaline electrolytes on Ni foil at 2.00 V<sub>RHE</sub> are shown, while the ‘no amino acid’ case represents 0.1 M KOH. For the “no amino acid” case, the charge efficiency associated with Ni dissolution was calculated from measured Ni<sup>2+</sup> concentrations (**Figure S27**, Institution 1). The remaining charge was attributed to O<sub>2</sub> evolution, as no NH<sub>3</sub> or NO<sub>2/3</sub><sup>-</sup> formation is expected in the absence of amino acids. Error bars represent standard deviation from up to n = 7 and n = 2 for glycine and lysine, respectively.



## Recommended practices for reporting of electrochemical amino acid conversion for ammonia recovery

Given the significant influence of the experimental parameters identified in this benchmarking effort, an experimental protocol (grey) together with additional considerations (blue) is proposed in **Figure 7**. Prior to experimentation, a consistent preparation procedure, comprising thorough cell cleaning and electrode polishing with freshly prepared electrodes for each experiment, is recommended to ensure reproducible conditions and to prevent contamination from previous runs. Particular attention should be paid to the reference electrode, which should be calibrated with respect to the electrolyte of interest to enable reliable comparison across experiments. During electrolysis, several diagnostic checks, such as cyclic voltammetry and solution resistance measurements via electrochemical impedance spectroscopy, can help ensure reproducible performance by identifying issues related to electrode and electrolyte quality, as well as cell assembly parameters such as electrode spacing. We also emphasize the importance of reporting  $iR$ -corrected potentials, noting that the resistance term  $R$  can depend strongly on cell geometry and assembly. More importantly, as demonstrated in the experimental assessment in **Figure 4**, parameters related to convection (e.g., stir bar size and rotation rate, gas bubbling) and electrode dimensions (e.g., area-to-volume ratio) should be fully reported.

For product quantification, we caution against the use of colorimetric methods for ammonia, nitrate/nitrite, and carbon product detection, as these techniques were shown to suffer from interferences arising from amino acids, metal ions, and reaction byproducts (see **Experimental Section**). In contrast,  $^1\text{H}$  NMR spectroscopy and ion chromatography were found to be reliable when implemented with consistent sample preparation protocols, including immediate electrolyte acidification and appropriate storage. Furthermore, while isotope labeling can provide valuable mechanistic insights, careful interpretation is required due to the presence of isotopic nitrogen impurities observed in this work (**Figure S17**). Finally, we recommend comprehensive reporting of scientifically relevant metrics, such as product distributions, Faradaic efficiencies toward nitrogen- and carbon-containing products, and electrode dissolution, together with the corresponding experimental condition. Particular attention is given to the reporting of pulsing experiments, as the methodology used to account for faradaic charge such as how capacitive currents are excluded and how anodic and cathodic charges are treated in efficiency calculations can significantly influence quantitative comparisons (**Figure 5**) and should therefore



be explicitly reported. Such standardized reporting is essential to enable meaningful cross-laboratory comparisons and will be critical for advancing our understanding of electrochemical ammonia recovery from amino acids and organic waste.

Finally, we discuss potential strategies to improve ammonia efficiency and electrode stability based on the trends identified in this work. First, we show that potential pulsing is effective in enhancing ammonia efficiency (**Figure 6**). Future efforts can focus on optimizing pulse parameters (potential, duration, and frequency), which have been shown in other systems (e.g., CO<sub>2</sub> reduction<sup>30,31</sup> and urea oxidation<sup>12,27</sup>) to improve selectivity and activity. Second, the observed coupling between ammonia production and Ni dissolution (**Figure 1** and **Figure 6**) also highlights a fundamental bottleneck. One potential strategy is to decouple amino acid activation (i.e., C-N cleavage) from ammonia stabilization. This may be achieved by leveraging molecular oxidants (e.g., OH<sup>-</sup>, H<sub>2</sub>O<sub>2</sub>)<sup>52,53</sup> to enable amino acid activation at lower potentials, as well as through electrolyte engineering with ionic additives that enhance solution-phase ammonia stability while maintaining environmental compatibility. More urgently, systematic assessment of Ni stability in real wastewater systems is needed, coupled with chemically resolved characterization of organic nitrogen beyond bulk metrics (e.g., total nitrogen). Notably, prior studies using complex sludge matrices have not reported significant Ni dissolution,<sup>12</sup> suggesting additional matrix effects and/or a surface passivation mechanism that warrants further investigation and may present opportunities for catalyst engineering.



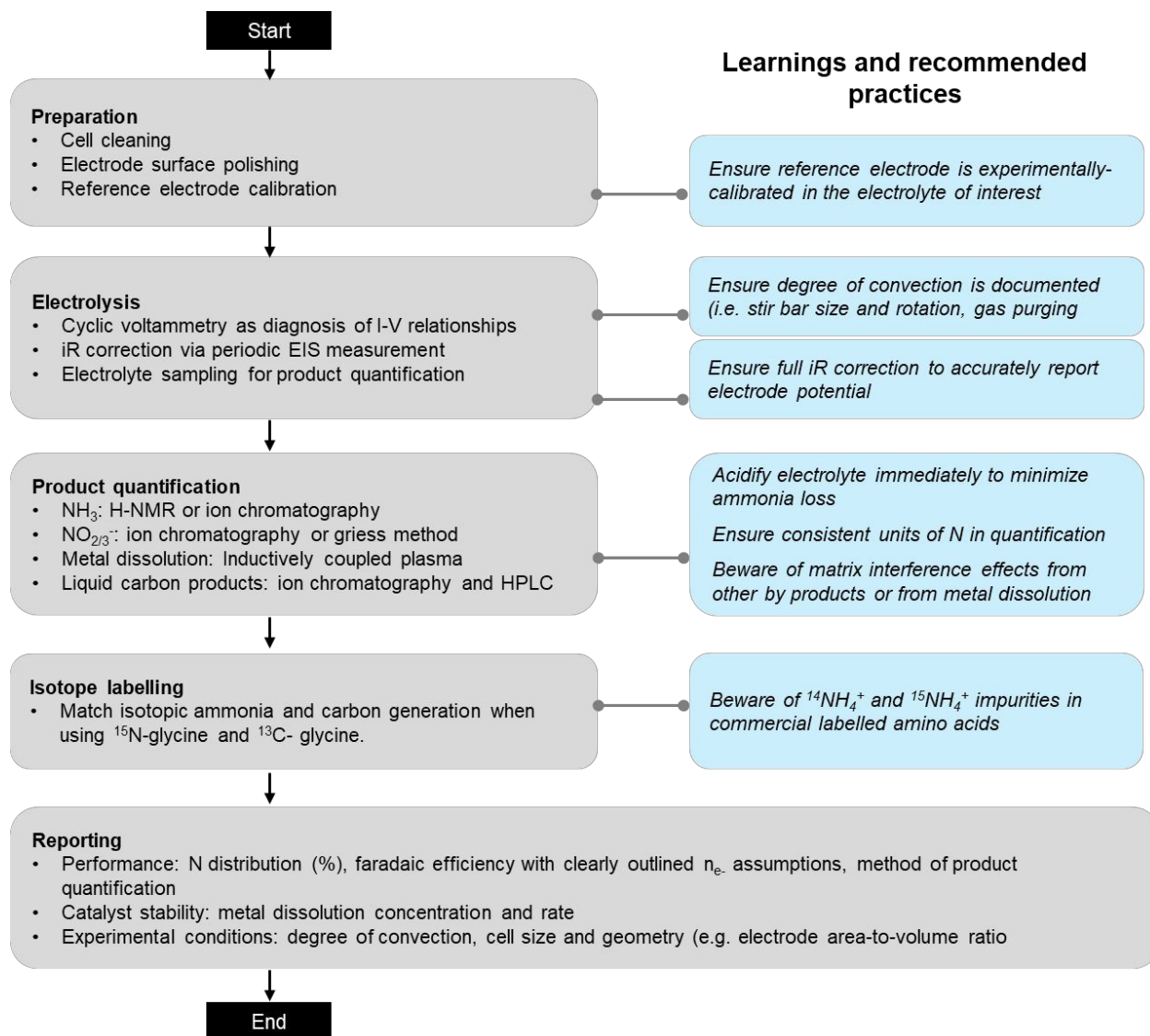


**Figure 7. Proposed experimental protocol** for the reliable electrochemical oxidation of glycine and other amino acids. Key learnings and recommended best practices at each stage, including cell and electrode preparation, electrochemical measurements, product detection, and isotope labeling, are summarized in blue on the right for consideration by researchers in the field.



## Conclusions

We have conducted a coordinated, cross-institutional study to elucidate the experimentally reproducible features of electrochemical glycine conversion to ammonia. By implementing an identical protocol using polished Ni foil in 0.1 M KOH containing 0.1 M glycine, we demonstrate that ammonia formation occurs under oxidative potentials ( $>1.60 V_{\text{RHE}}$ ), rather than under reducing conditions. Nevertheless, Ni exhibited the lowest overpotential for ammonia production compared to other electrodes, where ammonia was detectably produced only at  $>2.1 V_{\text{RHE}}$  and  $>2.6 V_{\text{RHE}}$  for Au and Pt, respectively. At  $2.00 V_{\text{RHE}}$  on Ni, ammonia constitutes the dominant solution-phase nitrogen product ( $\sim 70\%$  of the nitrogen product distribution), with a Faradaic efficiency of  $23.0 \pm 2.5\%$ . However, this selectivity is accompanied by substantial Ni dissolution. Comprehensive carbon product analysis of the electrolyte using HPLC, ion chromatography, and  $^{13}\text{C}$  NMR reveals the formation of multiple liquid-phase oxidation products, including glycolate, glyoxylate, formaldehyde, cyanide, and formate. Together, these products indicate the presence of parallel reaction pathways involving initial C-N cleavage (pathway 1) and C-C scission (pathway 2) during glycine activation. Complementary thermodynamic analysis further suggests that C-N cleavage may represent the rate-limiting step in both pathways, motivating targeted mechanistic investigations in future studies. Furthermore, extending the study to alanine, lysine, and aspartic acid reveals that ammonia-dominated production correlates with  $\text{Ni}^{2+}$  dissolution, highlighting Ni complexation as a possible origin of ammonia-dominated production. Importantly, nitrogen selectivity, Ni corrosion rates, and carbon product distributions were found to be highly sensitive to experimental parameters such as stirring rate, electrode area, cell architecture and potential pulsing. Specifically, pulsing to a negative potential was found to robustly increase the ammonia Faradaic efficiency (FE), with mechanistic implications of amine hydrogenation during C-N cleavage as the possible rate-limiting step, but the degree of FE enhancement is highly sensitive to how the positive and negative charges are accounted for. These observations highlight the critical role of the local reaction environment and underscore the need for exhaustive experimental reporting and community-facing best-practice protocols. Although this work focuses on simplified glycine and single-component amino acid systems, it serves as an important foundation for future studies to investigate electrode stability and ammonia production from more complex nitrogen



sources (e.g., proteins) and in the presence of other sludge constituents. Increasing system complexity will be essential to advance scalable ammonia recovery from organic waste.

## Contribution

A.J.M, Y.S-H and G.B. conceived the idea. H.I., J.A. and D.A.H.C. conducted benchmarking, product quantification and assessment of experimental factors, under the leadership of H.I. D.D.V. helped developed the institution's product quantification methodology. A.A. conducted pulsing experiments under the supervision of H.I. H.I., J.A. and D.A.H.C. prepared the initial draft. All authors were involved in editing and approving the final version of the manuscript.

## Acknowledgment

This work is based upon financial support by the National Science Foundation, EEC Division of Engineering Education and Centers, NSF Engineering Research Center for Advancing Sustainable and Distributed Fertilizer production (CASFER), NSF 20-553 Gen-4 Engineering Research Centers award # 2133576. H.I. gratefully acknowledges the financial support from the Martin Family Fellowship. D.A.C.H. was partially supported by RBI Graduate Research Fellowship from the Renewable Biproducts Institute at Georgia Institute of Technology. The authors thank Dr. Luisa Barrera and Dr. Nianhan (Kaylee) Tian for their work at the start of the project. Any opinions, findings, and conclusions or recommendations expressed in this material are those of the author(s) and do not necessarily reflect the views of the National Science Foundation.

## Data Availability

The data supporting the findings of this study are available in the Supplementary Information and from the corresponding authors upon reasonable request.

## Conflict of Interest

We declare no conflicts of interest.



## References

1. Zhou, Y., Zhu, Y., Zhu, J., Li, C. & Chen, G. A Comprehensive Review on Wastewater Nitrogen Removal and Its Recovery Processes. *Int J Environ Res Public Health* **20**, 3429 (2023).
2. Rahimi, S., Modin, O. & Mijakovic, I. Technologies for biological removal and recovery of nitrogen from wastewater. *Biotechnology Advances* **43**, 107570 (2020).
3. McCarty, P. L. What is the Best Biological Process for Nitrogen Removal: When and Why? *Environ. Sci. Technol.* **52**, 3835–3841 (2018).
4. Hu, X. *et al.* Effects of different external carbon sources and electron acceptors on interactions between denitrification and phosphorus removal in biological nutrient removal processes. *J. Zhejiang Univ. Sci. B* **19**, 305–316 (2018).
5. Rosso, D., Larson, L. E. & Stenstrom, M. K. Aeration of large-scale municipal wastewater treatment plants: state of the art. *Water Sci Technol* **57**, 973–978 (2008).
6. Botte, G. G. *et al.* Innovative Approach to Sustainable Fertilizer Production: Leveraging Electrically Assisted Conversion of Sewage Sludge for Nutrient Recovery. *ACS Omega* **9**, 49692–49706 (2024).
7. Chipoco Haro, D. A. *et al.* Electrocatalysts for Inorganic and Organic Waste Nitrogen Conversion. *ACS Catal.* **14**, 9752–9775 (2024).
8. Śpiwak, K. Gasification of Sewage Sludge—A Review. *Energies* **17**, (2024).
9. Trinh, T. N., Jensen, P. A., Dam-Johansen, K., Knudsen, N. O. & Sørensen, H. R. Influence of the Pyrolysis Temperature on Sewage Sludge Product Distribution, Bio-Oil, and Char Properties. *Energy Fuels* **27**, 1419–1427 (2013).



10. Yaala, M. B. *et al.* Plasma-assisted catalytic formation of ammonia in N<sub>2</sub>-H<sub>2</sub> plasma on a tungsten surface. *Phys. Chem. Chem. Phys.* **21**, 16623–16633 (2019).
11. Heberlein, J. & Murphy, A. B. Thermal plasma waste treatment. *J. Phys. D: Appl. Phys.* **41**, 053001 (2008).
12. Jafari, M. & Botte, G. G. Electrochemical valorization of waste activated sludge for short-chain fatty acids production. *Front. Chem.* **10**, (2022).
13. Singh, R. P. & Agrawal, M. Potential benefits and risks of land application of sewage sludge. *Waste Management* **28**, 347–358 (2008).
14. Kacprzak, M. *et al.* Sewage sludge disposal strategies for sustainable development. *Environmental Research* **156**, 39–46 (2017).
15. Hait, S. & Tare, V. Vermistabilization of primary sewage sludge. *Bioresource Technology* **102**, 2812–2820 (2011).
16. Collivignarelli, M. C. *et al.* What Advanced Treatments Can Be Used to Minimize the Production of Sewage Sludge in WWTPs? *Applied Sciences* **9**, (2019).
17. Gao, N., Kamran, K., Quan, C. & Williams, P. T. Thermochemical conversion of sewage sludge: A critical review. *Progress in Energy and Combustion Science* **79**, 100843 (2020).
18. Hui, W., Zhou, J. & Jin, R. Proteins recovery from waste activated sludge by thermal alkaline treatment. *Journal of Environmental Chemical Engineering* **10**, 107311 (2022).
19. Hoang, S. A. *et al.* Treatment processes to eliminate potential environmental hazards and restore agronomic value of sewage sludge: A review. *Environmental Pollution* **293**, 118564 (2022).
20. Vriens, L., Nihoul, R. & Verachtert, H. Activated sludges as animal feed: A review. *Biological Wastes* **27**, 161–207 (1989).



21. Marangoni, D. G., Smith, R. S. & Roscoe, S. G. Surface electrochemistry of the oxidation of glycine at Pt. *Can. J. Chem.* **67**, 921–926 (1989).
22. Sáez-Plaza, P., Michałowski, T., Navas, M. J., Asuero, A. G. & Wybraniec, S. An Overview of the Kjeldahl Method of Nitrogen Determination. Part I. Early History, Chemistry of the Procedure, and Titrimetric Finish. *Critical Reviews in Analytical Chemistry* **43**, 178–223 (2013).
23. Gootzen, J. F. E., Wonders, A. H., Visscher, W., van Santen, R. A. & van Veen, J. A. R. A DEMS and cyclic voltammetry study of NH<sub>3</sub> oxidation on platinumized platinum. *Electrochimica Acta* **43**, 1851–1861 (1998).
24. Huerta, F. *et al.* Electrochemical behaviour of amino acids on Pt(*h,k,l*): a voltammetric and in situ FTIR study. Part 1. Glycine on Pt(111). *Journal of Electroanalytical Chemistry* **421**, 179–185 (1997).
25. Chen, L.-C., Uchida, T., Chang, H.-C. & Osawa, M. Adsorption and oxidation of glycine on Au electrode: An in situ surface-enhanced infrared study. *Electrochemistry Communications* **34**, 56–59 (2013).
26. K. Boggs, B., L. King, R. & G. Botte, G. Urea electrolysis: direct hydrogen production from urine. <https://doi.org/10.1039/B905974A> (2009) doi:10.1039/B905974A.
27. Vedharathinam, V. & Botte, G. G. Understanding the electro-catalytic oxidation mechanism of urea on nickel electrodes in alkaline medium. *Electrochimica Acta* **81**, 292–300 (2012).
28. Laan, P. C. M. *et al.* Understanding the Oxidative Properties of Nickel Oxyhydroxide in Alcohol Oxidation Reactions. *ACS Catal.* **13**, 8467–8476 (2023).
29. Mohan, R. *et al.* Electrochemical Oxidation of Glycine with Bimetallic Nickel–Manganese Oxide Catalysts. *ChemElectroChem* **7**, 561–568 (2020).



30. Freer, W. H. *et al.* Ammonia production from pulsed electrolysis of amino acids. *J Appl Electrochem* **55**, 2561–2571 (2025).
31. Kimura, K. W. *et al.* Controlled Selectivity of CO<sub>2</sub> Reduction on Copper by Pulsing the Electrochemical Potential. *ChemSusChem* **11**, 1781–1786 (2018).
32. Huang, Y. *et al.* Pulsed electroreduction of low-concentration nitrate to ammonia. *Nat Commun* **14**, 7368 (2023).
33. Zheng, W. *iR* Compensation for Electrocatalysis Studies: Considerations and Recommendations. *ACS Energy Lett.* **8**, 1952–1958 (2023).
34. Wei, C. *et al.* Recommended Practices and Benchmark Activity for Hydrogen and Oxygen Electrocatalysis in Water Splitting and Fuel Cells. *Advanced Materials* **31**, 1806296 (2019).
35. Wan, H., Bagger, A. & Rossmeisl, J. Electrochemical Nitric Oxide Reduction on Metal Surfaces. *Angewandte Chemie International Edition* **60**, 21966–21972 (2021).
36. Iriawan, H. *et al.* Assessing the Activity of Transition Metal Oxides for the Electrochemical N<sub>2</sub> Oxidation to Nitrate. *ACS Catal.* **15**, 6315–6333 (2025).
37. Tatarchuk, S. W., Medvedev, J. J., Li, F., Tobolovskaya, Y. & Klinkova, A. Nickel-Catalyzed Urea Electrolysis: From Nitrite and Cyanate as Major Products to Nitrogen Evolution. *Angewandte Chemie International Edition* **61**, e202209839 (2022).
38. Thakkar, H. K. *et al.* Vertically Oriented FeNiO Nanosheet Array for Urea and Water Electrolysis at Industrial-Scale Current Density. *ACS Sustainable Chem. Eng.* **12**, 8340–8352 (2024).
39. Kiss, T., Sovago, I. & Gergely, A. Critical survey of stability constants of complexes of glycine. *Pure and Applied Chemistry* **63**, 597–638 (1991).



40. Varadwaj, P. R., Cukrowski, I. & Marques, H. M. DFT-UX3LYP Studies on the Coordination Chemistry of Ni<sup>2+</sup>. Part 1: Six Coordinate [Ni(NH<sub>3</sub>)<sub>n</sub>(H<sub>2</sub>O)<sub>6-n</sub>]<sup>2+</sup> Complexes. *J. Phys. Chem. A* **112**, 10657–10666 (2008).
41. Huang, L.-F., Hutchison, M. J., Santucci, R. J. Jr., Scully, J. R. & Rondinelli, J. M. Improved Electrochemical Phase Diagrams from Theory and Experiment: The Ni–Water System and Its Complex Compounds. *J. Phys. Chem. C* **121**, 9782–9789 (2017).
42. Hudson, R. *et al.* CO<sub>2</sub> reduction driven by a pH gradient. *Proceedings of the National Academy of Sciences* **117**, 22873–22879 (2020).
43. Shenderovich, I. G., Denisov, G. S., Shenderovich, I. G. & Denisov, G. S. NMR Properties of the Cyanide Anion, a Quasisymmetric Two-Faced Hydrogen Bonding Acceptor. *Symmetry* **13**, (2021).
44. Das, K., Dumais, J., Basiaga, S. & Krzyzanowski, G. D. Carbon-13 nuclear magnetic resonance analysis of formaldehyde free preservatives. *Acta Histochemica* **115**, 481–486 (2013).
45. Butch, C. *et al.* Production of Tartrates by Cyanide-Mediated Dimerization of Glyoxylate: A Potential Abiotic Pathway to the Citric Acid Cycle. *J. Am. Chem. Soc.* **135**, 13440–13445 (2013).
46. Cheng, S. C., Gattrell, M., Guena, T. & MacDougall, B. The electrochemical oxidation of alkaline copper cyanide solutions. *Electrochimica Acta* **47**, 3245–3256 (2002).
47. Xu, H., Li, A., Feng, L., Cheng, X. & Ding, S. Destruction of Cyanide in Aqueous Solution by Electrochemical Oxidation Method. *International Journal of Electrochemical Science* **7**, 7516–7525 (2012).



48. ZELITCH, I. & GOTTO, A. Properties of a new glyoxylate reductase from leaves. *Biochem J* **84**, 541–546 (1962).
49. Li, Y.-F. & Selloni, A. Mechanism and Activity of Water Oxidation on Selected Surfaces of Pure and Fe-Doped NiOx. *ACS Catal.* **4**, 1148–1153 (2014).
50. Son, Y. J. *et al.* Effects of Electrochemical Conditioning on Nickel-Based Oxygen Evolution Electrocatalysts. *ACS Catal.* **12**, 10384–10399 (2022).
51. Klaus, S., Cai, Y., Louie, M. W., Trotochaud, L. & Bell, A. T. Effects of Fe Electrolyte Impurities on Ni(OH)<sub>2</sub>/NiOOH Structure and Oxygen Evolution Activity. *J. Phys. Chem. C* **119**, 7243–7254 (2015).
52. Droz`d`z, R., Naskalski, J. W. & Sznajd, J. Oxidation of amino acids and peptides in reaction with myeloperoxidase, chloride and hydrogen peroxide. *Biochimica et Biophysica Acta (BBA) - Protein Structure and Molecular Enzymology* **957**, 47–52 (1988).
53. Stadtman, E. R. & Berlett, B. S. Fenton chemistry. Amino acid oxidation. *Journal of Biological Chemistry* **266**, 17201–17211 (1991).
54. Mahne, N. *et al.* Singlet oxygen generation as a major cause for parasitic reactions during cycling of aprotic lithium–oxygen batteries. *Nat Energy* **2**, 17036 (2017).
55. Chen, G. *et al.* A discussion on the possible involvement of singlet oxygen in oxygen electrocatalysis. *J. Phys. Energy* **3**, 031004 (2021).
56. A. Hansen, H., Rossmeisl, J. & K. Nørskov, J. Surface Pourbaix diagrams and oxygen reduction activity of Pt, Ag and Ni(111) surfaces studied by DFT.  
<https://doi.org/10.1039/B803956A> (2008) doi:10.1039/B803956A.



57. Trotochaud, L., Young, S. L., Ranney, J. K. & Boettcher, S. W. Nickel–Iron Oxyhydroxide Oxygen-Evolution Electrocatalysts: The Role of Intentional and Incidental Iron Incorporation. *J. Am. Chem. Soc.* **136**, 6744–6753 (2014).
58. Zilbermann, I., Maimon, E., Cohen, H. & Meyerstein, D. Redox Chemistry of Nickel Complexes in Aqueous Solutions. *Chem. Rev.* **105**, 2609–2626 (2005).
59. Green, B. J., Tesfai, T. M. & Margerum, D. W. Nickel(III) oxidation of its glycyglycylhistamine complex. *Dalton Trans.* 3508 (2004) doi:10.1039/b409929j.
60. Liu, X. *et al.* Interaction Structure and Affinity of Zwitterionic Amino Acids with Important Metal Cations ( $\text{Cd}^{2+}$ ,  $\text{Cu}^{2+}$ ,  $\text{Fe}^{3+}$ ,  $\text{Hg}^{2+}$ ,  $\text{Mn}^{2+}$ ,  $\text{Ni}^{2+}$  and  $\text{Zn}^{2+}$ ) in Aqueous Solution: A Theoretical Study. *Molecules* **27**, 2407 (2022).



## Data Availability

The data supporting the findings of this study are available in the Supplementary Information and from the corresponding authors upon reasonable request.

